Composition-structure-property effects of antimony in soda-lime-silica glasses

CHEN, Tzu-Yu, RAUTIYAL, Prince, VAISHNAV, Shuchi, GUPTA, Gaurav, SCHLEGL, Harald, DAWSON, Richard, EVANS, Adam, SAEED, Kamali, JACQUELINE, Johnson, CHARLES, Johnson and BINGHAM, Paul <http://orcid.org/0000-0001-6017-0798>

Published version

CHEN, Tzu-Yu, RAUTIYAL, Prince, VAISHNAV, Shuchi, GUPTA, Gaurav, SCHLEGL, Harald, DAWSON, Richard, EVANS, Adam, SAEED, Kamali, JACQUELINE, Johnson, CHARLES, Johnson and BINGHAM, Paul (2020). Composition-structure-property effects of antimony in soda-lime-silica glasses. Journal of Non-Crystalline Solids.

Composition-structure-property effects of antimony in soda-lime-silica glasses

T.-Y. Chen[1], P. Rautiyal[1], S. Vaishnav[1], G. Gupta[1,2], H. Schlegl[3], R. J. Dawson[3], A. W. Evans[4], S. Kamali[4], J. A. Johnson[4], C. E. Johnson[4] and P. A. Bingham[1,*]

[1] *Materials and Engineering Research Institute, College of Business, Technology and Engineering, Sheffield Hallam University, City Campus, Howard Street, Sheffield, S1 1WB, UK.*

[2] *Glass Division, Central Glass and Ceramic Research Institute, Raja S. C. Mullick Road, Kolkata, India*

[3] *Department of Engineering, Lancaster University, Lancaster, LA1 4YW, UK*

[4] *Department of Mechanical, Aerospace and Biomedical Engineering, University of Tennessee Space Institute, Tullahoma, TN 37388, USA.*

* Corresponding author, contact details: Email p.a.bingham@shu.ac.uk; Phone +44 1142256449

Abstract

Float glass-type SiO_2-Na_2O-CaO glasses with 0 – 10 mol% Sb_2O_3 were melted and their compositional, structural, thermal and optical properties characterised. All glasses were X-ray amorphous and increasing Sb_2O_3 content progressively decreased glass transition temperature (T_g) and dilatometric softening point (T_d), despite increases in Al_2O_3 content from greater crucible corrosion. ^{121}Sb Mössbauer spectroscopy confirmed that Sb was predominantly incorporated as Sb^{3+} ($Sb^{3+}/\Sigma Sb$ ~ 0.9) and Raman spectroscopy showed that Sb substantially decreased average (Si, Al)-O Q^n speciation. Both techniques confirmed that Sb^{3+} ions were incorporated in trigonal pyramidal [:SbO_3] polyhedra. XRF and Raman spectroscopies confirmed that SO_3 content decreased with increasing Sb_2O_3 content. TGA analysis showed, as a linear function of Sb_2O_3 content, mass gain commencing at 700°C, reaching a maximum at 1175°C, then mass loss above 1175°C, consistent with oxidation ($Sb^{3+} \rightarrow Sb^{5+}$) then reduction ($Sb^{5+} \rightarrow Sb^{3+}$). The TGA samples were shown to have attained or approached Sb redox equilibrium during measurement. Optical absorption spectroscopy (UV-Vis-nIR) showed red-shifts of the UV absorption edge with increasing Sb_2O_3 content, consistent with increasing intensity of far-UV absorption bands from Sb^{3+} and Sb^{5+} s→p transitions. UV-Vis-nIR fluorescence spectroscopy evidenced a broad luminescence band centred at ~25,000 cm^{-1}, attributed to the $^3P_1 \rightarrow {}^1S_0$ transition of Sb^{3+}, which is Stokes shifted by ~15,000 cm^{-1} from the $^1S_0 \rightarrow {}^3P_1$ absorption at ~40,000 cm^{-1}. The most intense emission occurred at 0.5 mol% Sb_2O_3, with concentration quenching reducing luminescence intensities at higher Sb_2O_3 contents. Additions of Sb_2O_3 to float-type soda-lime-silica glasses could thus enable lower melting energies and/or new solar energy applications.

1. Introduction

Antimony and arsenic oxides are historically among the most efficient and widely-used fining agents for aiding the removal of bubbles during melting of commercial soda-lime-silica glasses and other types of glass [1-7]. More recently, both Sb- and As-based refining agents have been replaced (largely on the basis of their toxicity [1, 2]) by sulphur-containing refining agents such as Na_2SO_4 and blast-furnace slag [1-4]. The combination of Sb and As oxides with nitrates in the raw materials mixture (batch) in 0.1-1 wt% quantities lead to particularly effective two-stage refining [2-4], whereby decomposition of alkali nitrates at intermediate temperatures (i.e. at an earlier stage of glass melting) releases large quantities of NO and O_2 gas, creating large bubbles which rapidly rise to the glass melt surface sweeping smaller bubbles with them; whilst also oxidising the Sb or As components as in (1), where R = alkali cation:

$$4RNO_3 + 2Sb_2O_3 \rightarrow 2R_2O + 2Sb_2O_5 + 4NO\uparrow + O_2\uparrow \qquad (1)$$

The reaction described by (1) is followed at higher temperatures (i.e. at later stages of glass melting) by reduction of the Sb_2O_5 or As_2O_5 according to (2), which releases further O_2 bubbles and thus provides further refining action:

$$Sb_2O_5 \rightarrow Sb_2O_3 + O_2 \qquad (2)$$

A criterion for a metal oxide, such as Sb or As, with two different oxidation states that are available under conditions accessible in glass making, to be active and effective as a fining agent, is the ability to release oxygen at a temperature that is not too high and not too low, so as to occur in the appropriate stages of glass melting. Arsenic, antimony and sulphur oxides are among the few known oxides which fulfil this criterion without colouring the glass [1-5]. Indeed, in addition to its efficacy as a refining agent, Sb has also been used as a decolourising and oxidising agent in glasses, from Roman times to the modern day [5, 8-15]. Soda-lime-silica glasses are often coloured by impurities (< ~0.1 wt%) of Fe and other transition metals such as Ti and Mn, which chiefly arise from the raw materials used in glass production. Iron, which is the most problematic from the viewpoint of unwanted colour, occurs in both Fe^{2+} and Fe^{3+} oxidation states in soda-lime-silica glasses and such glasses melted in air and under mildly oxidising conditions exhibit typical $Fe^{2+}/\Sigma Fe$ ratios of 0.1 – 0.4 [16, 17]. These Fe^{2+} and Fe^{3+} impurities can substantially affect optical absorption behaviour of the glass, with well-known oxygen-metal charge-transfer bands affecting UV absorption; and *d-d* absorption bands arising at visible and near-infrared wavelengths [5, 8, 17-19]. Antimony decolourises such glasses by oxidising Fe^{2+} to Fe^{3+} through mutual redox interactions during glass melting and cooling [5, 8-10, 15, 20, 21], whereby:

$$Sb^{5+} + 2Fe^{2+} \rightarrow Sb^{3+} + 2Fe^{3+} \qquad (3)$$

In addition to the study of antimony as a refining and decolourising agent, other effects of antimony in oxide glass have also received attention. Antimony oxide is a conditional glass former and simple binary SiO_2-Sb_2O_3 [22, 23], B_2O_3-Sb_2O_3 [24, 25] and P_2O_5-Sb_2O_3 [26] glasses, and more complex glasses [11, 13, 27-31], have all been studied to gain new and fundamental composition-structure-property understanding. Oxide glasses containing Sb_2O_3 as a major constituent exhibit novel optical properties [31-35], with high refractive indices [32, 34] and transparency to infrared radiation [32] making them potential candidate glasses for non-linear optical devices. There is also evidence that Sb_2O_3 can render oxide glasses more resistant to formation of high-energy radiation-induced defects [25, 29, 35] and thus Sb_2O_3 additions can provide enhanced shielding against γ-radiation [25].

Both Sb and As typically occur in multiple valence states in oxide glasses (Sb^{3+}/Sb^{5+} and As^{3+}/As^{5+}), but unlike many other well-known multivalent cations (e.g. most transition metals and several lanthanides) they do not generate absorption bands centred at visible or near-infrared energies. Even antimonate and arsenate glasses, wherein the major constituent is Sb_xO_y or As_xO_y, are yellow-gold in colour but remain transparent [25, 31- 34]. This yellow-gold colouration is caused by far-UV absorption bands which produce tails that reach visible energies [36-42]. Following photon absorption, vibrational losses in the oxide glass host lead to Stokes Shifts and re-emission of a portion of the absorbed energy as photons with lower energies, some at visible wavenumbers. Enhanced UV absorption, coupled with re-emission of a proportion of the absorbed energy as lower-energy (visible) photons, is a combination that could have particular advantages in certain solar energy applications [43, 44].

The research presented here is part of a wider study with the joint aims of: (i) improving understanding of the composition-structure-property effects of antimony additions to soda-lime-silica glasses representative of current commercial glass compositions; and (ii) establishing whether additions of antimony to soda-lime-silica glasses can provide new functionalities and applications; and greater stability in extreme environments. The first part of this study, presented here, focuses on composition-structure-property effects. The second part will be presented in a forthcoming publication.

2. Experimental Procedures

Batches to provide 200 g of glass were produced using raw materials of ≥99·9% purity sand (SiO_2), aluminium hydroxide ($Al(OH)_3$), magnesium carbonate ($MgCO_3$), calcium carbonate ($CaCO_3$), sodium carbonate (Na_2CO_3), sodium sulphate (Na_2SO_4) and antimony oxide (Sb_2O_3). Raw materials were dried at 110°C for at least 24 h prior to weighing and mixing. Batches were weighed into sealed polymer bags using a calibrated 3 decimal place balance. Once weighing was complete, the bags were sealed and batches were thoroughly mixed in a figure-of-eight motion for at least 3 minutes to ensure good mixing of all raw materials. The antimony-free glass had a nominal composition representative of commercial float-type soda-lime-silica glass [1, 2]. Antimony was supplied to the batches as Sb_2O_3, which was added on a pro-rata molar basis at levels of 0.5, 1, 5 and 10 mol% Sb_2O_3. Consequently the glass samples with 0, 0.5, 1, 5, and 10 mol% Sb_2O_3 were labelled Sb0, Sb0.5, Sb1, Sb5 and Sb10 respectively. The mixed batches were placed in recrystallized Al_2O_3 crucibles, which were then placed in an electric furnace and heated at a rate of 5°C min^{-1} to 1450°C, then held at this temperature for 5 h. The crucibles were then removed from the furnace and the melts were poured into steel moulds on a steel plate and allowed to cool until sufficiently stiff to remove the moulds without flow of the cooling melt. The glasses were then immediately placed in an electric furnace at 530°C and held at this temperature for 1 h to relieve thermal stresses, then cooled slowly within the furnace to room temperature. The nominal compositions of all glasses (mol%) are given in Table 1.

For measurements by X-ray diffraction and X-ray fluorescence and ^{121}Sb Mössbauer spectroscopies, powdered samples were prepared in a vibratory disc mill. X-ray diffraction (XRD) was carried out using an Empyrean PANalytical diffractometer in Bragg–Brentano geometry with Co K_{a1} (1.78897 Å) radiation, operating at 40 kV and 40 mA on a spinner stage, with a step size of 0.001° 2θ. All obtained diffraction patterns are shown in Figure 1.

Chemical compositions of all glasses were analysed using a Philips Magix Pro X-ray fluorescence spectrometer. Fused beads were made by mixing the powdered sample and lithium tetraborate flux in a 1:10 ratio. Beads were melted in a Pt/5%Au crucible at 1065°C for 15 min before being air cooled. An in-house quantitative XRF Wide-Range Oxide analysis program, OXI, was used to analyse XRF data [45]. The analysed compositions of all glasses (mol%) are given in Table 1. The estimated uncertainties associated with the XRF OXI program-analysed compositions are ± 0.05 % for minor oxides (< 1 mol% abundance); ± 0.10 % for middle oxides (1 - 10 mol% abundance); and ± 0.20 % for major oxides (>10 mol% abundance).

Densities were measured on samples of ~10 g bulk glass using the Archimedes method in deionised water at 22.5 ± 1°C, assuming a density of water 0.9976 g cm^{-3}. Density values were calculated using the expression $\rho = (m_d / m_{d\text{-}}m_w) \times \rho_{water}$, where m_d = weight of the dry sample and m_w = weight of the immersed sample. Averages of three measurements were taken for each sample. All measured densities are given in Table 1. Uncertainties were conservatively estimated to be ±0.005 g cm^{-3} to incorporate any human, instrumental and sample errors / uncertainties. Molar volumes for each glass, also given in Table 1, were calculated using the analysed compositions and measured densities, according to (4):

$$V_m = m_m / \rho \qquad (4)$$

where V_m = molar volume / $cm^3\ mol^{-1}$; m_m = molar mass / g mol^{-1}; and ρ = density / g cm^{-3}. The estimated uncertainties incorporate density and XRF uncertainties, and consequently they increase with increasing Sb_2O_3 content of the glass.

^{121}Sb Mössbauer spectroscopy was performed on powdered samples Sb5 and Sb10 using an MS4 spectrometer operating in constant acceleration mode in transmission geometry at room temperature (293K, 20°C) using a $Ca^{121}Sn$ source. All centre shifts, δ, were measured with respect to metallic α-Fe at room temperature. The velocity scale was determined by iron calibration, hence the absolute source velocity must be slightly adjusted because an $Rh^{57}Co$ source has an isomer shift relative to α-Fe. This correction requires subtraction of 0.1 mm s^{-1}. Next, the centre shift values were converted to give values relative to InSb by adding 8.6 mm s^{-1}, to enable direct comparisons with the literature. Hence the conversion was -0.1+8.6 = +8.5 mm s^{-1}. Spectra were least-square fitted to extract the hyperfine parameters centre shift (δ), quadrupole interaction (e^2Qq), Lorentzian linewidth (Γ), and intensities (I). Both spectra, which are best fitted with two sub-spectra, are illustrated in Figure 2. The velocity scale shown in Figure 2 is the as-measured velocity scale and does not incorporate the aforementioned velocity-scale conversions. The asymmetry in the larger component is due to the presence of eight lines in the $7/2^+$ to $5/2^+$ transition in ^{121}Sb. The extracted Mössbauer parameters for both spectra, which include the converted centre shift (δ) values, are given in Table 2.

All Raman and UV-Vis-nIR optical absorption and fluorescence spectroscopy measurements were carried out on polished samples. Samples were cut, ground and polished to 3 - 4 mm thickness (also typical of commercial float glass) with SiC grinding papers in decreasing particle sizes from 125 μm to 15 μm, and then polished with a suspension of CeO_2 polishing media to give a mirror-polished surface (< 1 μm).

UV-Vis-nIR absorption spectra were collected using a Varian Cary 50 Scan UV-visible spectrophotometer over the range 10,000 – 50,000 cm^{-1} (1000 – 200 nm) at a scan rate of 60 nm min^{-1}, and with a data interval of 0.5 nm. Baseline and background scans were performed prior to sample runs to provide accurate data correction. Measured absorption data was corrected to a path length of 1 mm and all spectra are shown in Figure 3.

UV-Vis-nIR fluorescence spectroscopy was performed using a Varian Cary Eclipse fluorescence spectrophotometer. All samples of bulk glass were placed in the spectrometer at 30° to the excitation source and were excited at 40,000 cm^{-1} based on the known energy of the $^1S_0 \rightarrow {}^3P_1$ transition of Sb^{3+} in similar oxide glasses [36-42]. Excitation and emission slits were both set at 5 nm and the detector voltage was 615 V. Excitation interference was minimised by an excitation bandpass filter (40,000 – 25,316 cm^{-1}) and an emission bandpass filter (33,898 – 9,090 cm^{-1}). All samples were measured in emission mode from 33,333 – 9,090 cm^{-1} with a scan rate of 120 nm min^{-1}, a data interval of 1 nm and an averaging time of 0.5 s. All luminescence spectra are shown in Figure 4.

Raman spectroscopy was performed using a Thermo Scientific DXR^{TM}2 spectrometer with a depolarised 10 mW 532 nm laser, on flat and polished bulk samples of all glasses, over a spectral range of 200 – 2000 cm^{-1}. Calibrations and laser alignment with the proprietary Thermo auto-alignment tool using a polystyrene film were carried out prior to sample data collection. Background subtractions and baseline corrections were carried out using the Thermo software smart background removal tool, and a 5th polynomial baseline correction method, respectively. Data were then corrected for temperature and excitation line effects, following the widely-used methodology (see, for example, [47-49]) which is based on the approach developed by Long [50]. The corrected Raman spectra for all samples are presented in Figure 5, in which all corrected spectra were normalised to an intensity of 1 for the peak at ~1100 cm^{-1}. Figure 6 shows difference spectra obtained by subtracting the corrected, normalised Raman spectrum for the Sb0 antimony-free glass from the other corrected, normalised sample spectra.

Dilatometric measurements were performed using a Netzsch Expedis Select DIL 402 dilatometer in air at a heating rate of 5°C min^{-1}. Regular glass cuboids of dimensions 5 mm × 5 mm × 25 mm were prepared for dilatometry. The glass transition temperature (T_g), dilatometric softening temperature (T_d) and coefficient of thermal expansion between 150°C and 400°C ($\alpha_{150\text{-}400°C}$) were determined for all glasses. Uncertainties associated with measured T_g and T_d (±5°C each) were estimated from repeated measurements of the same sample and from temperature calibration of the instrument using an Al_2O_3 standard material. All corrected dilatometry traces are shown in Figure 7 and the extracted T_g, T_d and $\alpha_{150\text{-}400°C}$ are given in Table 3.

Simultaneous TGA and DSC analyses were carried out using a Netzsch STA 449 F3 Jupiter simultaneous thermal analyser. Powdered samples were loaded into Al_2O_3 sample pans and heated in air at 10°C min^{-1} from 20°C to 1250°C. DSC traces became progressively less detailed with increasing sample Sb_2O_3 content, and samples Sb5 and Sb10 did not provide measurable values of T_g. The obtained DSC T_g values and estimated uncertainties are given in Table 3. Note that the heating rate used for these measurements was different to that used for the dilatometric measurements. As discussed by Fluegel [46], it is well known that measured values of T_g depend on heating rate, however, Fluegel [46] also noted that the difference in heating rates that we have used here (dilatometry 5°C min^{-1} and DSC/TGA 10°C min^{-1}) is appropriate, and enables direct comparison between T_g values extracted from dilatometry and DSC data. The T_g values from the two different techniques, given in Table 3, can thus be considered comparable. TGA data is shown in Figure 8, and mass gain between 700°C and 1175°C as a function of analysed Sb_2O_3 content of the glass is illustrated in Figure 9, which also shows molar volumes (V_m) as a function of analysed Sb_2O_3 content.

3. Results

3.1. Phase, Composition, Density and Molar Volume Analyses

Figure 1 shows the diffraction patterns for all glass samples. Only amorphous humps were obtained with no sharp peaks, confirming that all samples were X-ray amorphous. The angle (°2θ) corresponding to the maximum intensity of the amorphous hump shifted to larger angles (°2θ) with increasing Sb_2O_3 content of the glass, from 29.0±1°2θ (Sb0) to 29.5±1°2θ (Sb0.5), 30.0±1°2θ (Sb1), 30.5±1°2θ (Sb5) and 32.0±1°2θ (Sb10).

The nominal composition, XRF analysed composition, measured density and molar volume of each sample are shown in Table 1. As expected on the basis of the high atomic mass of Sb, glass densities increase from ~2.5 to g cm^{-3} ~3.0 g cm^{-3} with increasing Sb_2O_3 concentration from 0 to 10 mol%. Analysed glass compositions are, in general, in close agreement with nominal compositions. However, increasing contents of Al_2O_3 (arising from increasing levels of crucible corrosion with increasing Sb_2O_3 contents) were detected, reaching high levels (~7 to ~12 mol%) in the Sb5 and Sb10 samples. Incorporation of this additional Al_2O_3 in the glass led to corresponding decreases in the analysed contents of the other constituents, with particular impact on the compositions of the Sb5 and Sb10 samples. Molar volume (V_m) remained approximately constant for Sb_2O_3 contents of up to 1 mol%, then V_m increased linearly from 1 to 10 mol% Sb_2O_3 content, suggesting possible changes in the structure of the glass and / or the local environment of Sb^{3+}/Sb^{5+} at a point between 1 and 5 mol% Sb_2O_3. The shift, with increasing Sb_2O_3 content, in the diffraction angle (°2θ) at which the amorphous hump has its maximum (see above) is also qualitatively consistent with corresponding changes in the composition and / or structure of the glass. Impurity levels (≤0.01 mol%) of Fe_2O_3 were also detected in the glasses by XRF (Table 1). These impurities are believed to have originated from the raw materials, principally the silica sand, used to prepare the glasses.

Figure 1. *X-ray diffraction (XRD) patterns for all glasses. Note shift in amorphous hump.*

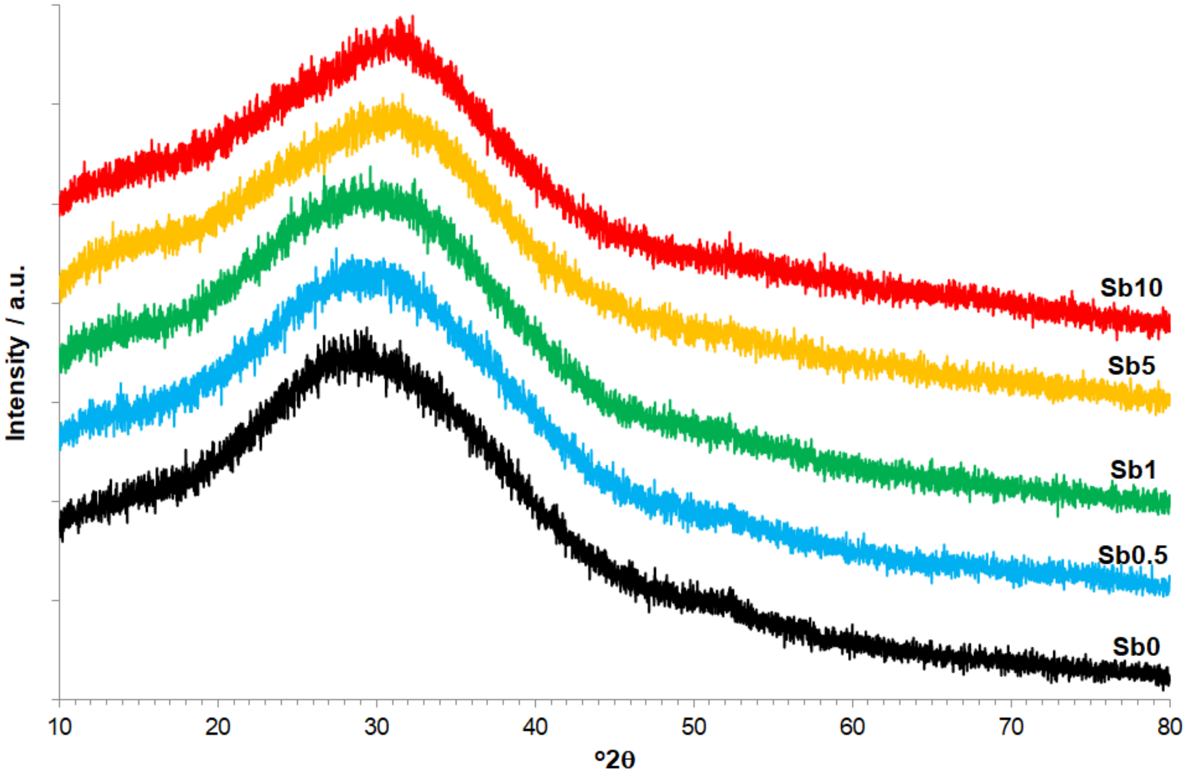

Table 1. *Nominal and analysed compositions (mol%) and measured densities and molar volumes of all glasses (Nom. nominal; An. Analysed).*

Glass	**Sb0**		**Sb0.5**		**Sb1**		**Sb5**		**Sb10**	
Mol%	**Nom.**	**An.**	**Nom.**	**An.**	**Nom.**	**An.**	**Nom.**	**An.**	**Nom.**	**An.**
Na_2O	13.76	13.41	13.69	13.38	13.62	13.19	13.07	12.07	12.38	10.86
MgO	5.49	3.94	5.46	3.85	5.44	3.85	5.22	3.37	4.94	2.94
Al_2O_3	0.59	0.76	0.59	0.97	0.58	1.18	0.56	6.94	0.53	11.62
Fe_2O_3	0.00	0.01	0.00	0.01	0.00	0.00	0.00	0.00	0.00	0.01
SiO_2	70.67	71.73	70.32	71.34	69.96	70.92	67.13	63.50	63.60	56.43
SO_3	0.22	0.18	0.22	0.13	0.22	0.11	0.21	0.03	0.20	0.00
CaO	9.27	9.96	9.22	9.84	9.18	9.75	8.81	8.84	8.35	7.60
Sb_2O_3	0.00	0.00	0.50	0.49	1.00	1.00	5.00	5.26	10.00	10.54
Total	100.00	100.00	100.00	100.00	100.00	100.00	100.00	100.00	100.00	100.00
ρ / g cm^{-3}	2.499 ± 0.005		2.537 ± 0.005		2.603 ± 0.005		2.839 ± 0.005		3.002 ± 0.005	
V_M / cm^3 mol^{-1}	23.8 ± 0.10		23.98 ± 0.10		23.85 ± 0.15		26.22 ± 0.25		29.49 ± 0.50	

3.2. ^{121}Sb Mössbauer Spectroscopy

Figure 2 shows the fitted ^{121}Sb Mössbauer spectra obtained from the Sb5 and Sb10 glasses, and Table 2 shows all fitted parameters. The two fitted spectra are closely similar in profile, component areas and fitted parameters. Spectra exhibit two major components, characteristic of Sb^{3+} (broad asymmetric component) and Sb^{5+} (narrow symmetric component) [23, 24, 26, 30, 51, 52]. The Sb^{5+} has a Kr electron configuration with a filled *d*-shell (d^{10}), i.e. it is spherical and therefore has no electric field gradient at the nucleus, so any quadrupole interaction observed for Sb^{5+} will be small compared to that for Sb^{3+}; or it will be zero. In some of the previous ^{121}Sb Mössbauer studies of oxide glasses the quadrupole interaction for Sb^{5+}, $e^2Qq(Sb^{5+})$, was either constrained to a value of zero [51, 52], or no quadrupole interaction for Sb^{5+} was observed [26], with those authors noting that this component can be fitted with a singlet-line quadrupole model. Other researchers have fitted this component with a small quadrupole interaction of $e^2Qq(Sb^{5+}) \approx 3$ to 6 mm s^{-1} [23, 24]. However, it was noted that "no reliable value could be obtained" [24] and that "this is difficult to separate from the linewidth contribution and is of doubtful accuracy" [23]. Similarly-mixed results were obtained by Stewart *et al.* [53] who studied several different antimony oxides and found that whilst α-Sb_2O_4 and $Sb_2O_5.3.61H_2O$ produced fitted spectra with $e^2Qq(Sb^{5+}) = -6.1$ mm s^{-1} and -4.3 mm s^{-1}, respectively, β-Sb_2O_4, $Sb_2O_5.3.56H_2O$ and Sb_6O_{13} all produced no visible asymmetry so those spectra were fitted with single lineshapes. In the present study we were able to successfully fit spectra with a single-line quadrupole model for Sb^{5+}, however, given the signal-to-noise ratios for the measured spectra (Figure 2) a quadrupolar component with a small value of $e^2Qq(Sb^{5+})$ could also have been fitted whilst achieving equivalent values of χ^2 for the fits.

This study has not directly established the recoil-free fractions, *f*, for Sb^{3+} and Sb^{5+} in the glasses studied, and consequently it cannot be stated with certainty that the ratio of recoil-free fractions, $f(Sb^{3+}) / f(Sb^{5+}) = 1$. However, there is some evidence to suggest that the value is close to 1. In their ^{121}Sb Mössbauer study of several different oxides of antimony, Stewart *et al.* [53] noted that "while in general this assumption can by no means be taken for granted, there are grounds for believing that for the compounds investigated here it cannot be far wrong and leads to reasonably realistic independent estimates of the Sb^{III}:Sb^{V} ratios". Holland *et al.* [24] confirmed, through variable-temperature measurements of a 60 Sb_2O_3 – 40 B_2O_3 (mol %) glass, that the relative intensities of Sb^{3+} and Sb^{5+} remained approximately constant, i.e. $f(Sb^{3+}) / f(Sb^{5+}) \approx 1$, between 10K and 77K. Mee *et al.* [23] reached a similar conclusion from measurements at 77K of cervantite ($Sb_2O_4 \equiv Sb^{3+}Sb^{5+}O_4$). However, they also described unpublished research which indicated that Sb_2O_3-B_2O_3 glasses exhibited a ~20% increase in Sb^{3+} relative intensity on cooling from 77K to 10K. This appears to contradict the results of Holland *et al.* [24] and the two findings are not easy to reconcile. It is possible that there may have been significant differences in: (1) the compositions (i.e. Sb_2O_3/B_2O_3 ratio) of the glasses; and / or (2) the Sb^{3+} / Sb^{5+} redox ratios in the glasses; and / or other differences. However, our measurements were made at 293K, and this must be considered against the lower-temperature measurements from the literature. De Laune *et al.* [54] studied $FeSb_2O_4$ and noted a difference in relative Sb^{3+} and Sb^{5+} absorption areas at 90K and 293K, such that the apparent Sb^{5+} fraction increased from 18% to 22%. They stated that at 90K the recoil-free fractions, f, for Sb^{3+} and Sb^{5+} were similar but the difference in apparent Sb^{5+} fraction at ambient temperature was expected because of the significantly higher Debye-Waller factor for Sb^{3+} compared with Sb^{5+}, and the resulting lower recoil-free fraction at ambient temperatures for Sb^{3+} compared with Sb^{5+}. Hence, we can surmise that the published research for oxide glasses and Sb_2O_4 [23, 24, 53] support the view that the recoilless fraction ratio $f(Sb^{3+}) / f(Sb^{5+}) \approx 1$ for those materials, measured between 10K and 77K. However, for the samples measured at 293K in this study, according to the literature $f(Sb^{3+}) / f(Sb^{5+})$ at 293K may vary slightly from a value of 1 (see, for example, [54]) and consequently the $Sb^{3+}/\Sigma Sb$ ratios derived here from the Sb^{3+} and Sb^{5+} spectral component areas have greater uncertainties than the corresponding fitted spectral peak areas.

Figure 2. *Fitted ^{121}Sb Mössbauer spectra (293K) for samples Sb5 and Sb10, each showing two fitted components representing Sb^{3+} (blue line) and Sb^{5+} (red line).*

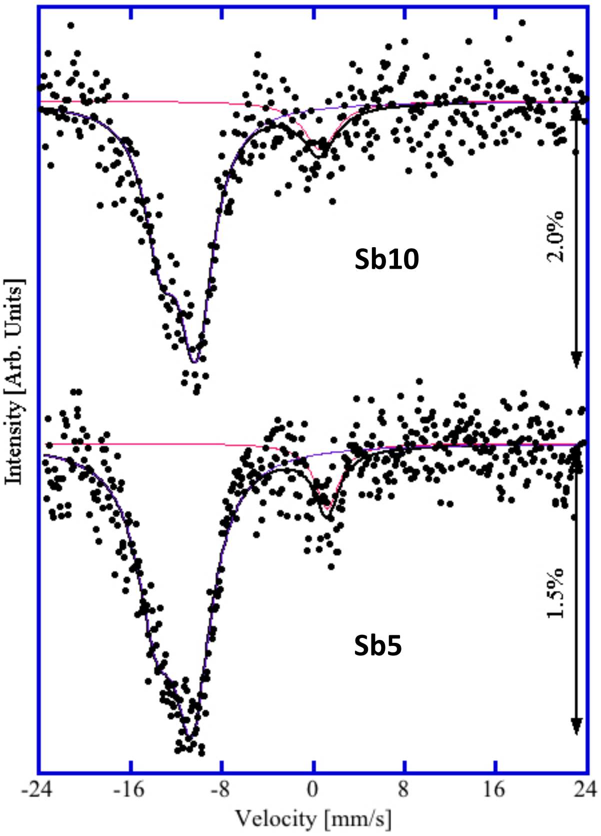

Table 2. *Refined ^{121}Sb Mössbauer parameters (293K): centre shift relative to InSb* (δ), *quadrupole interaction* (e^2Qq), *Lorentzian linewidth* (Γ), *intensity* (I). *Bracketed numbers are uncertainties in the first decimal place.*

Glass	**Sb5**	**Sb10**
δ_1 / mm s^{-1}	-3.6(2)	-3.2(3)
e^2Qq_1 / mm s^{-1}	19.5(9)	18.9(9)
Γ_1 / mm s^{-1}	4.0(4)	3.5(4)
I_1 / %	90(3)	88(3)
δ_2 / mm s^{-1}	9.7(4)	9.1(8)
Γ_2 / mm s^{-1}	2.6(7)	3.5(6)
I_2 / %	10(3)	12(3)
Peak absorption / %	1.5	2.0

3.3. Optical Absorption and Fluorescence Spectroscopies

All glass samples were optically transparent, with colours ranging from colourless (Sb0) to light yellow (Sb10), with increasing depth of the colour accompanying increasing Sb_2O_3 content. Figure 3 displays the UV-Vis-nIR absorption spectra of the five studied glasses. The most notable feature is a red-shift of the absorption edge, of the order of 4500 cm^{-1}, which corresponds with increasing Sb_2O_3 content from sample Sb0 to Sb10. Also of note, and shown in the inset in Figure 3, very weak and narrow absorption bands (labelled Fe^{3+}) are observed in the spectra for samples Sb0, Sb0.5 and Sb1 at ~ 26,500 cm^{-1}, ~ 24,000 cm^{-1}, ~ 23,000 cm^{-1} and a very weak, broad band (labelled Fe^{2+}) is centred at ~ 10,500 cm^{-1} in the spectrum for sample Sb0. The band at ~ 10,500 cm^{-1} is only observed for sample Sb0 and disappears upon addition of Sb_2O_3 to the glass; whilst the bands at ~ 26,500 cm^{-1}, ~ 24,000 cm^{-1} and ~ 23,000 cm^{-1} can be observed for samples Sb0, Sb0.5 and Sb1, i.e. up to Sb_2O_3 contents of 1 mol%. These bands have been attributed to the Fe_2O_3 impurities (≤ 0.01 mol%) detected in the glasses (Table 1).

Figure 3. *UV-Vis-nIR absorption spectra corrected to 1 mm path length (inset: weak Fe^{3+} and Fe^{2+} absorption bands highlighted)*

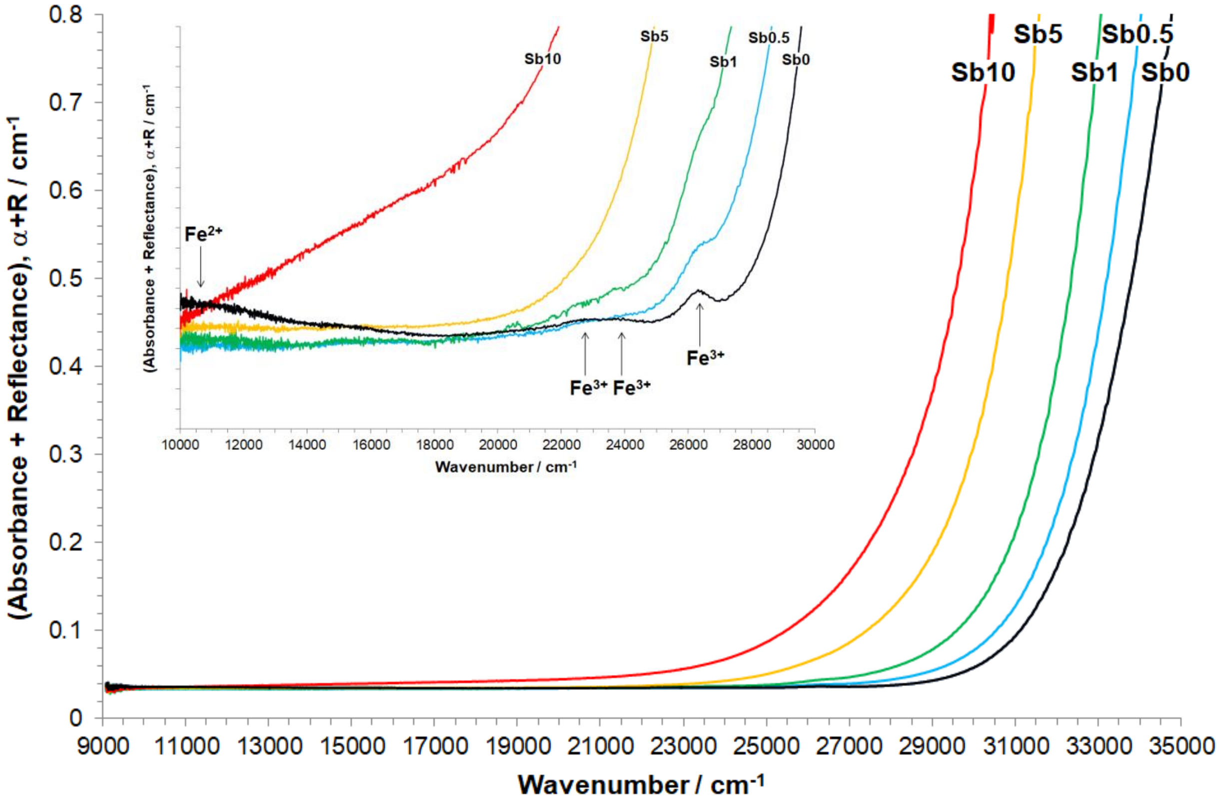

The UV-Vis-nIR luminescence spectra are shown in Figure 4. A broad luminescence band, centred at 25,200 – 25,600 cm^{-1}, is present in spectra for all Sb-containing glasses, suggesting that all bands are due to the same transition. Intensity of this luminescence band decreases in the order Sb0.5 > (Sb1 ≈ Sb5) > Sb10.

Figure 4. *UV-Vis-nIR luminescence spectra (excitation at 40,000 cm^{-1})*

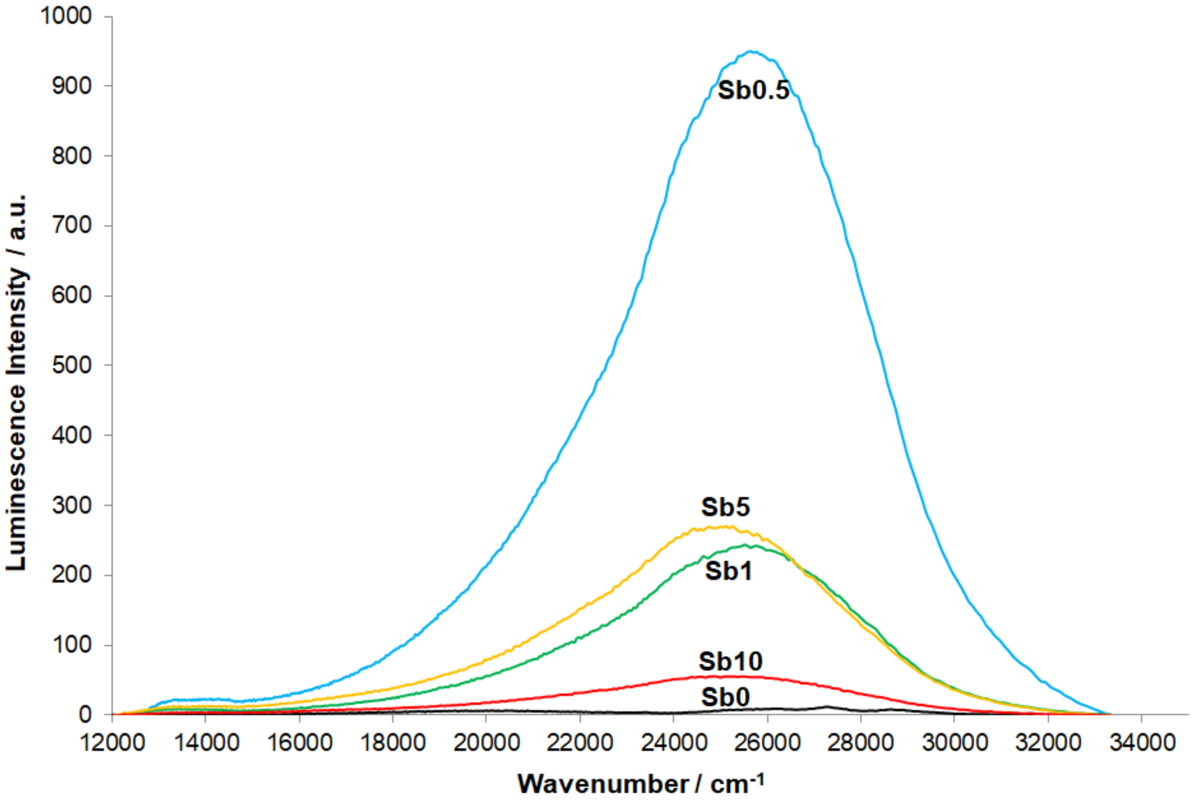

3.4. Raman Spectroscopy

A stacked plot of the corrected Raman spectra for all samples is given in Figure 5. A plot showing the difference in Raman intensity between corrected, normalised (to the peak near 1100 cm^{-1}) spectra for each Sb-containing glass from the spectrum for the Sb0 antimony-free glass is given in Figure 6. The Raman spectra for all samples can be split into two major regions: the lower-frequency region (200 – 750 cm^{-1}) and the higher-frequency region (750 – 1400 cm^{-1}). The addition of Sb_2O_3 to the batches not only affected Sb_2O_3 contents of the glasses, it also affected Al_2O_3 and SO_3 contents (Table 1) and these changes must also be taken into account when considering the effects of

Sb_2O_3 additions on the Raman spectra. As shown in both Figures 5 and 6, increasing (Sb_2O_3 + Al_2O_3) content led to small spectral changes up to 1 mol% Sb_2O_3. These changes become more pronounced at 5 and 10 mol % Sb_2O_3. However, changes to the Raman spectra occur at all Sb_2O_3 contents and these changes show consistent trends for all Sb_2O_3 contents studied. The difference spectra in Figure 6 qualitatively illustrate these changes, which are summarised as follows:

i) 1075 – 1250 cm^{-1}, decrease in intensity centred at ~1100 cm^{-1}

ii) 850 – 1075 cm^{-1}, increase in intensity centred at ~1020 cm^{-1}; dip at 990 cm^{-1} and shoulder at ~920 cm^{-1}

iii) 200 – 850 cm^{-1}, two new bands arise at ~700 cm^{-1} and ~510 cm^{-1}

Figure 5. *Corrected Raman spectra, intensity-normalised to peak ~ 1100 cm^{-1}*

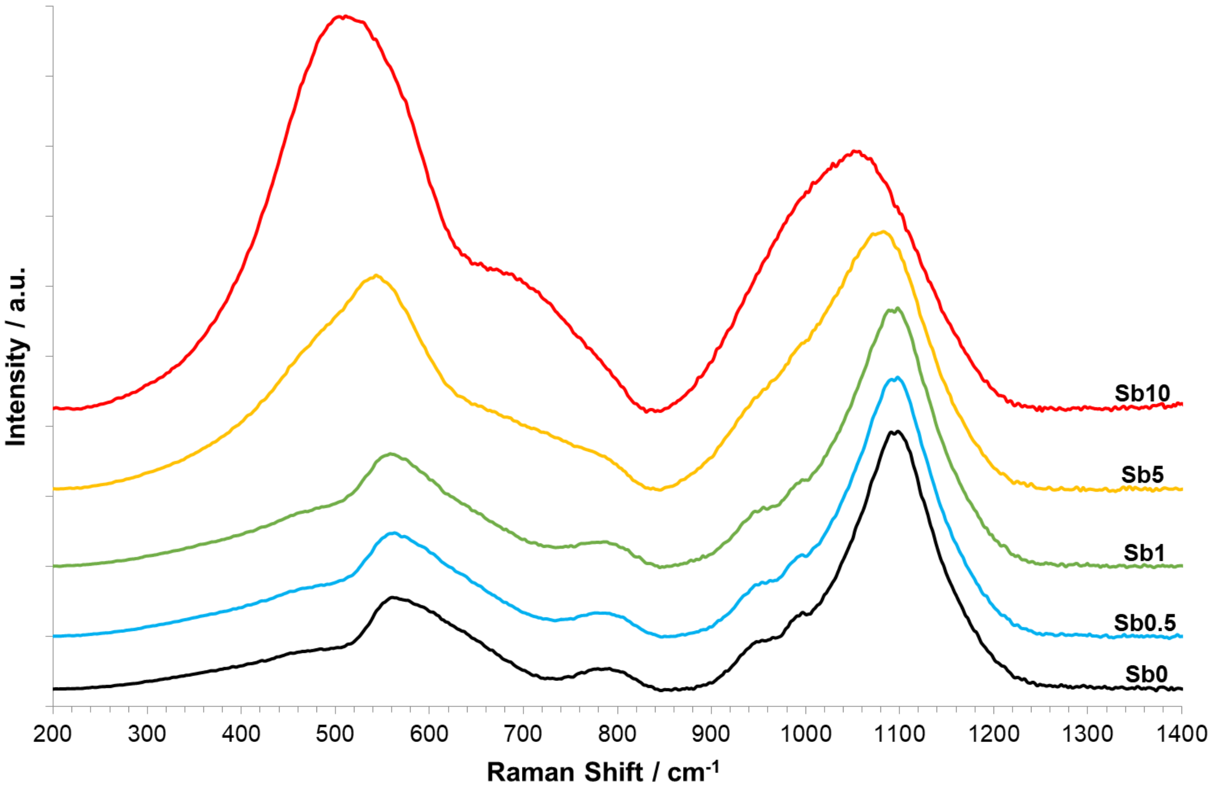

Figure 6. *Difference Raman spectra of corrected data, intensity-normalised to peak at ~1100 cm^{-1}*

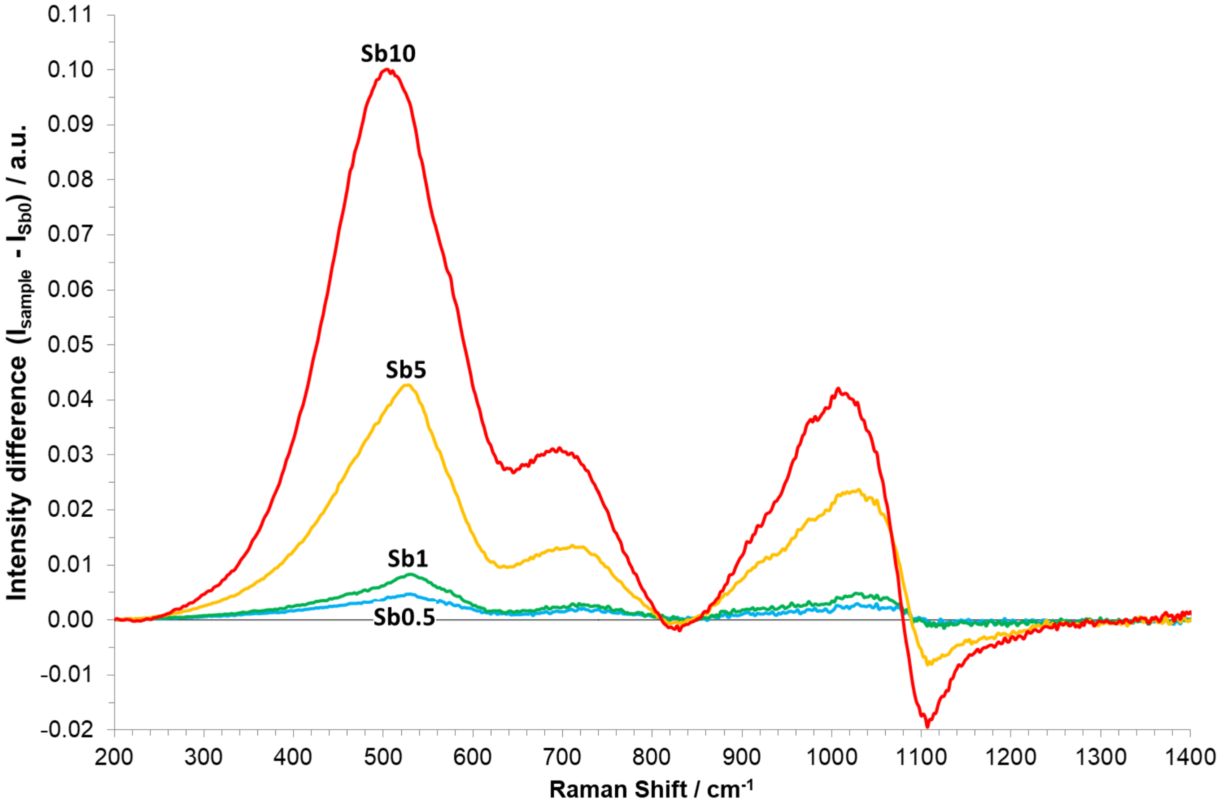

3.6. Thermal Analysis

Dilatometry data for all samples are shown in Figure 7. The extracted coefficient of thermal expansion between 150°C and 400°C ($\alpha_{150\text{-}400^{\circ}C}$), onset glass transition temperatures obtained from both dilatometry and DSC (T_g), and the dilatometric softening temperature (T_d) are shown in Table 3. Addition of (Sb_2O_3 + Al_2O_3) to the glass had no net effect on the coefficient of thermal expansion, which remained essentially constant for all samples studied. The additional Al_2O_3 presumably arose from enhanced crucible corrosion during glass melting, as confirmed by XRF analysis (Table 1). The onset glass transition temperature, T_g, decreased with increasing (Sb_2O_3 + Al_2O_3) content, from ~560°C for sample Sb0 to ~500°C for sample Sb10. Similarly, the dilatometric softening temperature (T_d) decreased with increasing (Sb_2O_3 + Al_2O_3) content, from ~615°C for sample Sb0 to ~555°C for sample Sb10.

Figure 7. *Dilatometry data for all glasses. Onset T_g and T_d are marked.*

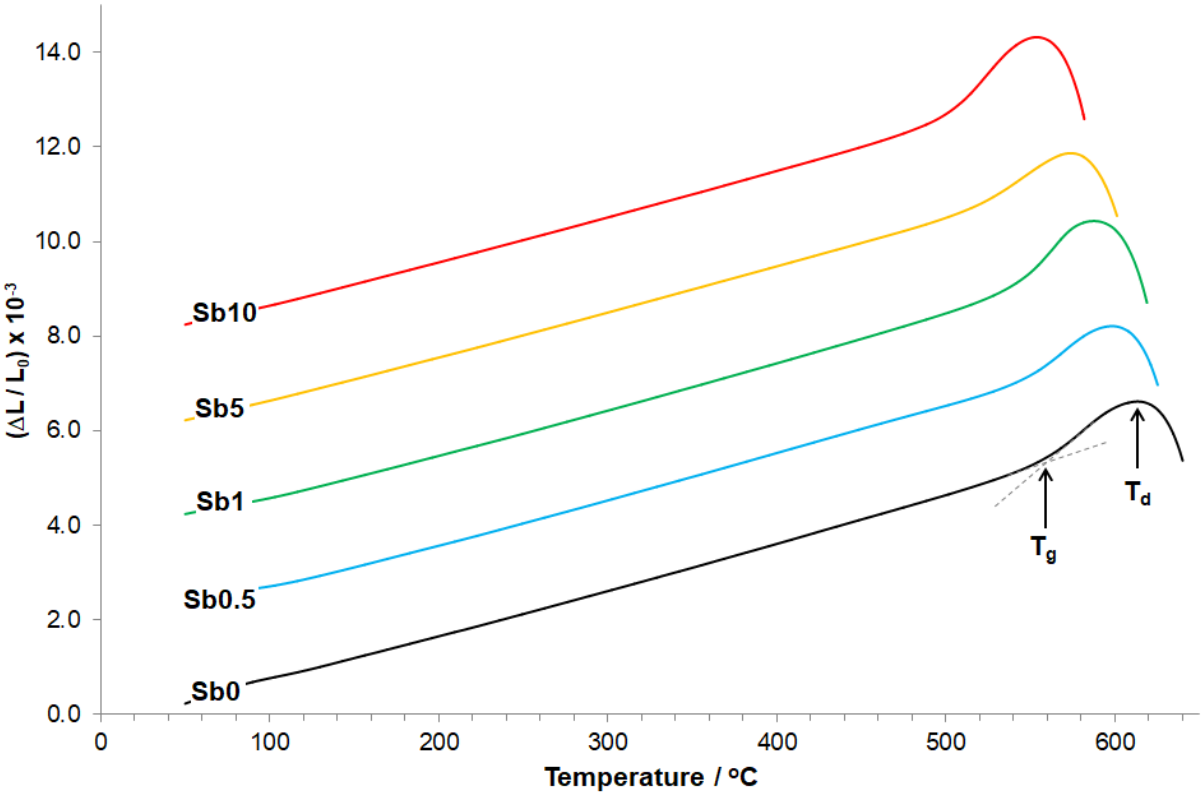

Table 3. *Measured glass thermal properties: onset glass transition temperatures (T_g) obtained from dilatometry and DSC; dilatometric softening temperature (T_d) and coefficient of thermal expansion (CTE, $\alpha_{150\text{-}400\ °C}$).*

Glass	**$T_{g\ (Dil.)}$ ± 5 / °C**	**$T_{g\ (DSC)}$ ± 10 / °C**	**T_d ± 5 / °C**	**(α x 10^{-7}) ± 2.0 / °C^{-1}**
Sb0	560	563	614	96.6
Sb0.5	549	558	598	96.8
Sb1	544	543	588	96.7
Sb5	522	-	574	95.7
Sb10	503	-	554	96.0

TGA data for all samples, measured between 50°C and 1250°C, are shown in Figure 8. Weight gain occurs at temperatures above ~700°C for Sb_2O_3-containing samples, reaching a maximum weight at ~1175°C, followed by weight loss at temperatures above ~1175°C. As shown in Figure 9, the maximum weight gain demonstrates a linear relationship with the analysed Sb_2O_3 content of the glass, indicating a direct relationship.

Figure 8. *TGA weight change of glasses as a function of temperature*

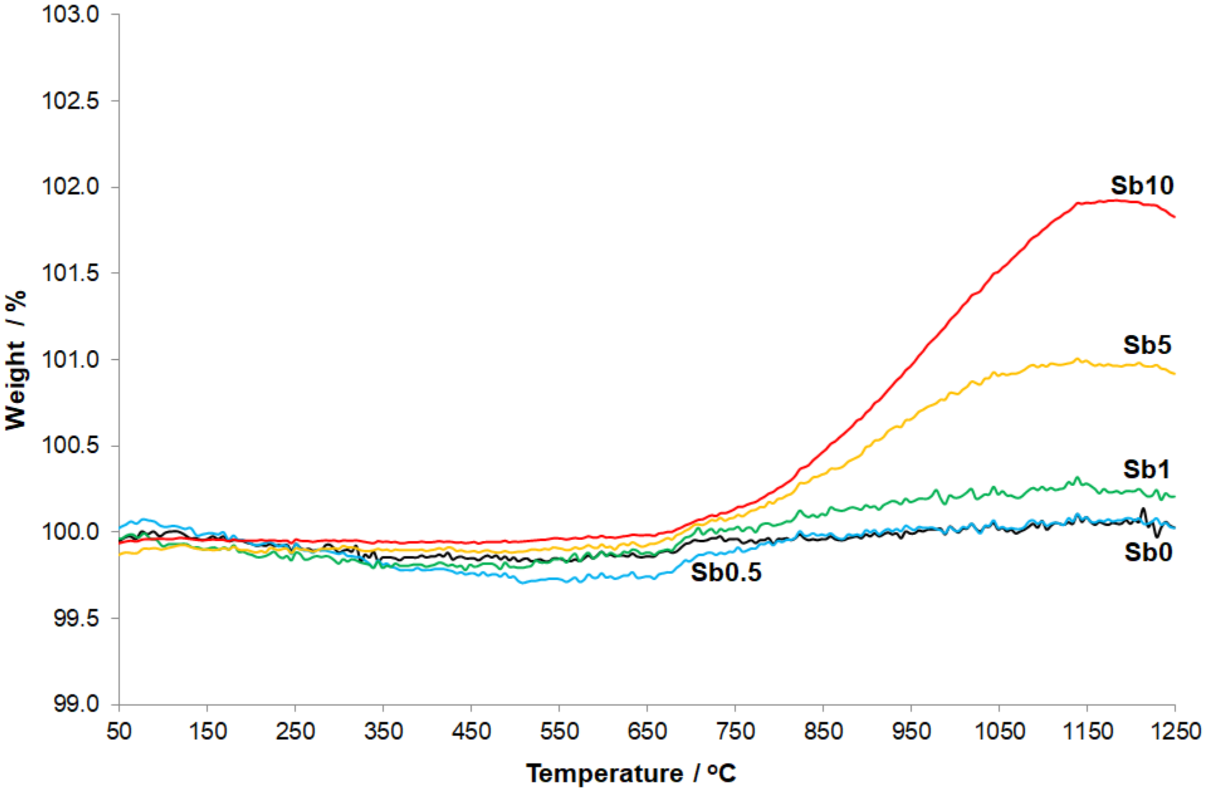

Figure 9. *Molar volume (V_m) and TGA weight gain (700°C – 1175°C) as functions of analysed Sb_2O_3 content. Linear fit (solid line, R^2 shown) and guide (dotted line) shown.*

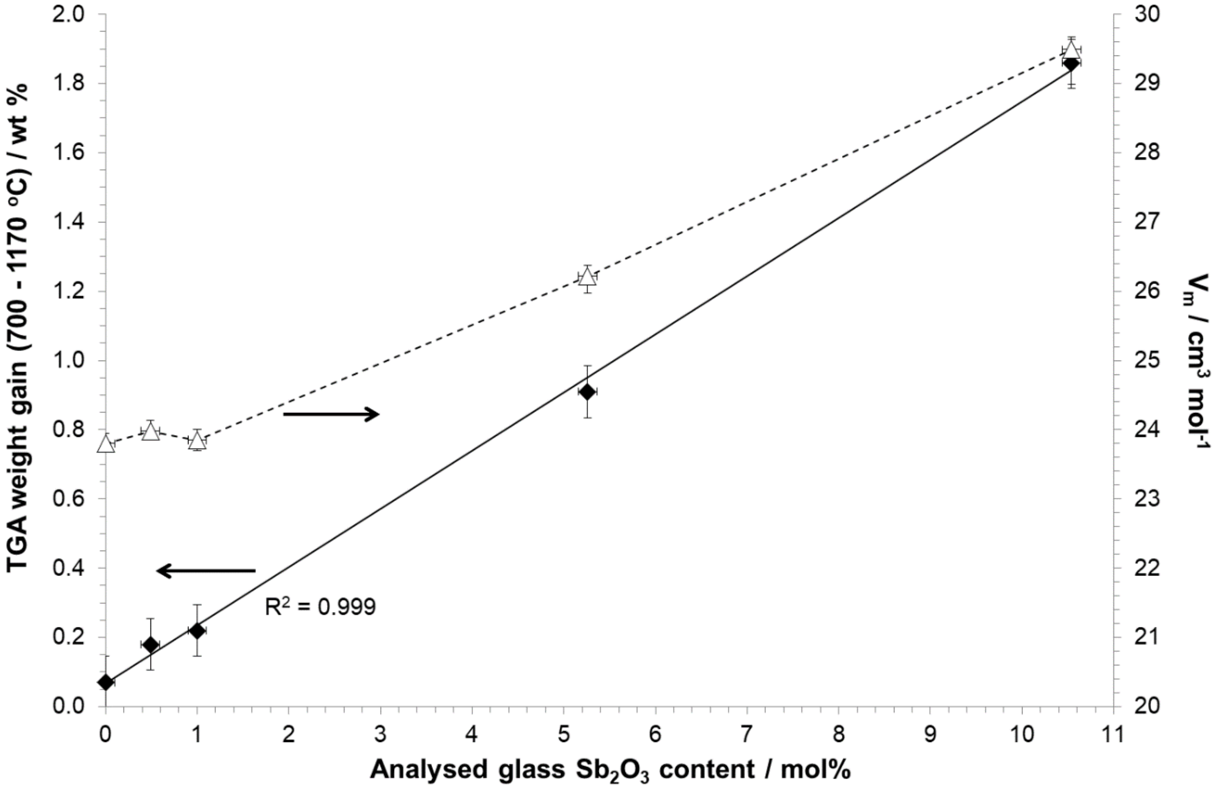

4. Discussion

4.1. Composition-Viscosity Relations

The addition of Sb_2O_3 to soda-lime-silica glasses representative of float glass compositions produces a myriad of changes to their chemical, structural, optical and thermal properties. Some of these changes are combined with the effects of increased Al_2O_3 content. As shown in Table 1, increasing Sb_2O_3 content of the glass was accompanied by increased Al_2O_3 content, particularly for the Sb5 and Sb10 samples, which had roughly comparable molar contents of Sb_2O_3 and Al_2O_3. This additional Al_2O_3 can only have arisen from increased corrosion of the recrystallized Al_2O_3 crucibles used to melt the glasses, and is consistent with Sb_2O_3 substantially decreasing the glass melt viscosity and / or surface tension during melting. Both of these can cause enhanced refractory corrosion [55]. For surface tension, Rubenstein [56] estimated that Sb_2O_3 modestly increases surface tension of soda-lime-silica type glass melts at 1200°C. This would suggest that surface tension effects are less likely to have caused the elevated Al_2O_3 contents in the glasses studied here.

Oxide glasses rich in Sb_2O_3 are known to exhibit low melting temperatures and low melt viscosities [57], consistent with the low melting temperature of pure Sb_2O_3 (656°C). The effects of Sb_2O_3 on the high-temperature viscosity of silicate glasses was studied by Fluegel *et al.* [58], who showed that Sb_2O_3 has a strong effect on decreasing television (TV) glass viscosity in the softening range ($\log(\eta$ / dPa s$) = 7\text{-}10$). This behaviour may reasonably be extrapolated to higher temperatures and other silicate glasses. It is also qualitatively consistent with the thermal analysis results for our glasses, which show substantial decreases in T_g and T_d with increasing (Sb_2O_3 + Al_2O_3) contents (Figure 7 and Table 3). This effect of Sb_2O_3 is all the more remarkable because it is in opposition to the effects of the elevated Al_2O_3 contents accompanying the Sb_2O_3 additions. The effects of Al_2O_3 on the viscosity of soda-lime-silica glasses are well-known and can be accurately modelled [1, 46, 58-60]. We have used Fluegel's model [46, 60] to predict the viscosity-temperature profiles for the analysed compositions of glasses Sb0 and Sb5, in order to understand the independent effect of Al_2O_3 and thus, indirectly, the effect of Sb_2O_3. For glass Sb5, the Sb_2O_3 content was neglected and other constituents increased on a *pro-rata* basis to total 100% for the purpose of modelling. Glass Sb10 could not be accurately modelled as the Al_2O_3 content for this glass lay outside the boundaries of model validity [46, 60]. The modelled results for our glasses show that addition of Al_2O_3 strongly increases melt viscosity, as expected. The melting temperature (at which log (η / dPa s) = 2) of glass Sb0 is 1450°C and by comparison (and neglecting Sb_2O_3), for glass Sb5 it is 1555°C, an increase of over 100°C. Correspondingly, the Littleton Softening Point (at which log (η / dPa s) = 7.6) is 727°C (glass Sb0) and 777°C (glass Sb5), a difference of 50^{o}C; and differences remain considerable, even at higher viscosities. For example, (log (η / dPa s) = 10) is 630°C for glass Sb0 and 673°C for glass Sb5; (log (η / dPa s) = 11) is 600°C for glass Sb0 and 641°C for glass Sb5; and (log (η / dPa s) = 13) is 553°C for glass Sb0 and 591°C for glass Sb5. The modelled viscosities given above for glass Sb0 are closely consistent with the measured T_d (614°C, corresponding to log (η / dPa s) ≈ 10 to 11) and measured onset T_g (560°C, corresponding to log (η / dPa s) = 13). However, the measured and modelled values for the Sb-containing glasses diverge greatly, owing to the model neglecting Sb_2O_3. Whilst the model indicates that for glass Sb5, T_d and T_g should increase to ~660°C and ~590°C, respectively, on account of its higher Al_2O_3 content, the measured T_d and T_g of 574°C and 522°C, respectively, are considerably lower than those for the Sb0 glass. This demonstrates the strong fluxing effects of Sb_2O_3 in these glasses, such that for a nominal 5 mol% addition, it effects net reductions in T_d of (660 – 574 ≈ 85°C) and in T_g of (590 – 522 ≈ 70°C). This fluxing effect is evidenced by the measured and modelled thermal properties. It also helps to explain the significant enhancement of Al_2O_3 crucible corrosion during glass melting due to a substantially lowered melt viscosity (see [55]), leading to elevated Al_2O_3 contents in the resulting glasses. The T_g of pure Sb_2O_3 glass is 250°C [22] and even for a binary 80 SiO_2 – 20 Sb_2O_3 (mol %) glass T_g remains very low, at ~335°C [22, 23]. The observed effect of Sb_2O_3 in strongly decreasing T_g (Table 3) is also consistent with a large body of literature for low-T_g glasses in a range of silicate [22, 23], borate [22, 24, 57], phosphate [26, 27], and antimonate [32, 34] glasses, all of which show consistently low T_g's.

4.2. Glass Structure

The incorporation of Sb_2O_3 in silicate glasses, commensurately with its effects on thermal properties, has substantial effects on glass structure. This is illustrated by the changes observed in the X-ray diffraction amorphous hump position with increasing (Sb_2O_3 + Al_2O_3) content shown in Figure 1. Whilst it is not possible to separate the effects of Sb_2O_3 and Al_2O_3 on the amorphous hump position without further research, the shift of the hump position to higher angles ($^o2\theta$) is consistent with some combination of shorter average interatomic bond distances and changes in X-ray scattering intensities. Other composition-structural indicators are density and molar volume (Table 1, Figure 9). Both increase with increasing Sb_2O_3 content. However, these changes are not linear and, as above, the effects of elevated Al_2O_3 contents must also be taken into consideration. As shown in Figure 9, the molar volume of the glasses is largely unaffected by Sb_2O_3 additions up to Sb_2O_3 contents between 1 and 5 mol%. At levels above this, the molar volume increases approximately linearly with Sb_2O_3 addition (further research is required to establish the exact Sb_2O_3 content at which this change in behaviour occurs and its structural origins). Such changes in behaviour may be indicative of changes in coordination, local environment, local clustering of Sb cations in the glass, or other effects. In order to confirm that these changes in V_m arose from Sb_2O_3 additions, and not to the elevated Al_2O_3 contents that accompany them in our glasses, we have used a similar approach to that used for thermal properties in Section 4.1 above. We calculated molar volumes (V_m) for the glasses whilst neglecting their Sb_2O_3 contents, using analysed compositions (Table 1) and Fluegel's robust and widely-used glass density model [46, 61]. This model shows that V_m would slightly decrease from its measured value of 23.8 cm^3 mol^{-1} (note: the modelled value for glass Sb0 was 23.9 cm^3 mol^{-1}, validating the accuracy of the model), to a modelled V_m of 23.0 cm^3 mol^{-1} for glass Sb10 (neglecting its Sb_2O_3 content). This modelled value takes account of the high Al_2O_3 content of this glass but ignores Sb_2O_3, and shows that Al_2O_3 incorporation in the glass has little effect on the molar volume of these glasses – the effect of Al_2O_3 is thus at least an order of magnitude smaller than that of Sb_2O_3 on a mole-for-mole basis. Given the large increases in V_m arising upon incorporation of (Sb_2O_3 + Al_2O_3), shown in Table 1 and Figure 9, the observed trends in V_m can thus be attributed predominantly to the incorporation of Sb_2O_3.

The Raman spectral region for oxide glasses between ~850 cm^{-1} and ~1200 cm^{-1} has been widely associated with T–O stretching modes (where T = Si, Al, Fe and others) of tetrahedrally-coordinated species [43, 47-49, 62-69]. The Q^n notation is also widely used to indicate network connectivity, where n = number of bridging oxygens per tetrahedron. Hence if more than one type of tetrahedral species, for example both SiO_4 and AlO_4^-, are present they will all contribute in this spectral region. Consequently the Q^n notation and Raman peaks in this spectral region apply to both SiO_4 and AlO_4^- units in the glasses studied here. Raman spectroscopy does not distinguish between Si- or Al- based tetrahedra in this regard [48]. Spectral contributions arising from different T-O (Q^n) units have been widely associated with peaks at certain Raman shifts, from Q^4 (~1150 cm^{-1}) to Q^3 (~1100 cm^{-1}), Q^2 (~950 cm^{-1}), Q^1 (~850 cm^{-1}) and Q^0 (~800 cm^{-1}) [43, 47-49, 62-69]. Spectral deconvolutions have also been carried out in this region (see, for example, [47-49, 64, 65, 67-69]) with variations in the nature, number and characteristics of the peaks fitted. For example, additional peaks have been assigned at ~1050 cm^{-1} and 800 cm^{-1} in different interpretations and deconvolutions of silicate glass Raman spectra [48, 64, 65, 67-69]. Some have attributed them to the stretching T_{2s} vibrational mode of TO_2 units [48] and some to Si–O stretching vibrations of bridging oxygens (BO) in SiO_4 tetrahedral units with at least one non-bridging oxygen (NBO) [65], respectively. Others have fitted two Q^3 components: one each for NBO's stabilised by alkali and alkaline earth cations [67]; and yet others have introduced a parameter Q_{ab}, where 'a' denotes a central tetrahedron type and 'b' denotes the nearest tetrahedron type, indicative of mid-range order [68]. Hence, whilst there is generally a degree of consensus in the literature regarding the deconvolution of Raman spectra in terms of Q^{0-4} units, there remain more subtle differences in the extracted information relating to spectral deconvolution in the Q^n region. It is known from ^{29}Si MAS-NMR studies of SiO_2-Na_2O-CaO glasses compositionally similar to our Sb0 glass that the only Si Q^n species present in this glass should be Q^3 and Q^4 [65, 66, 70, 71]. Raman bands associated with Sb-O units in glass have been reported by a number of authors [22, 23, 30, 72-74], but there is no evidence of Sb-O bands overlapping with the T-O Q^n region, making interpretation of the effects of Sb_2O_3 on glass structure slightly less challenging. The incorporation of Sb_2O_3 and the associated increase in Al_2O_3 content of our glasses, from Sb0 to Sb10, lead to several changes in their structure, illustrated in the Raman spectra (Figures 5 and 6). With increasing (Sb_2O_3 + Al_2O_3) content the Raman intensity centred at ~1100 cm^{-1} decreases, and the intensity at ~1020 cm^{-1} and ~920 cm^{-1} increases. This indicates decreases in the average Q^n of T-O species (SiO_4 and AlO_4^-) with increasing (Sb_2O_3 + Al_2O_3) content. Whilst the addition of Al_2O_3 to the glass on a pro rata basis (which approximates what occurred to the glasses studied here during melting) would be expected to result in a more polymerised network, i.e. an increase in average T-O Q^n, the substantial decrease in Raman intensity (Figure 6) at 1100-1150 cm^{-1} indicates decreases in the abundance of both (Si + Al) Q^4 and Q^3 species. These changes are accompanied by substantial increases in Raman intensity (Figure 6) between 850 cm^{-1} and 1050 cm^{-1}, with growth of peaks at ~920 cm^{-1} and ~1020 cm^{-1} which are consistent with increases in the abundance of (Si + Al) Q^2 species; and increased intensity (abundance) of the stretching T_{2s} vibrational mode of TO_2 units [48]. These changes, upon additions of Al_2O_3, are qualitatively different from the results of Le Losq *et al.* [48], who studied the effects of increasing Al_2O_3 content in SiO_2-Al_2O_3-Na_2O glasses and concluded that increasing the Al / (Al + Na) ratio produces a decrease in the proportion of Q^3 units but an overall increase in the proportion of Q^4 units. However, our glasses also contain Sb_2O_3 which therefore clearly has a profound effect. Our results, which suggest decreases in both Q^3 and Q^4 intensity and an increase in Q^2 intensity, therefore support the view that Sb_2O_3 plays a major role in (alumino)silicate network (de)polymerisation. It can thus be suggested that increasing (Sb_2O_3 + Al_2O_3) in our glasses led to substantial net (Si, Al) network depolymerisation. This is particularly illustrative of the strong depolymerising effect of Sb_2O_3 in silicate glasses, in light of the substantially increased Al_2O_3 content for samples Sb5 and Sb10 which would normally be expected to cause a re-polymerising effect on the network, with a resulting increase in the average Q^n as illustrated by Le Losq *et al.* [48]. However, the opposite appears to occur here, with a substantial decrease in the average Q^n. This result is consistent with the effects on thermal properties discussed in Section 4.1, which also confirm the effects of Sb_2O_3 in readily negating and overcoming the (re)polymerising effects of increased Al_2O_3. In order to further elucidate this behaviour, solid-state NMR experiments would prove beneficial.

The Raman band at 990 cm^{-1} can be unequivocally ascribed to the ν_1 symmetric S-O stretching modes in SO_4^{2-} units, as widely reported for silicate, aluminosilicate and borosilicate glasses [75-79]. This band gradually disappeared with increasing Sb_2O_3 additions, as shown in Figures 5 and 6. XRF analysis of the glasses (Table 1) confirmed increasing loss of SO_3, presumably as SO_2 gas, with increasing (Sb_2O_3 + Al_2O_3) content. This loss of sulphate is consistent with the disappearance of the SO_4^{2-} Raman band at 990 cm^{-1} with increasing (Sb_2O_3 + Al_2O_3) content. The mechanism by which the (Sb_2O_3 + Al_2O_3) accelerates or enhances sulphate loss is not yet clear but may involve viscosity, solubility, mutual redox reaction and / or surface tension effects, which are also discussed in Section 4.3.

The lower-frequency Raman region (200-800 cm^{-1}) contains many overlapping contributions associated with bending modes of SiO_4 tetrahedra [65, 66]. This spectral region for the Sb0, Sb0.5 and Sb1 glasses comprise a relatively narrow band centred at ~800 cm^{-1}, a broad asymmetric band with a peak at ~560 cm^{-1}, and a weak shoulder at ~460 cm^{-1}. This is consistent with Raman spectra obtained for other SiO_2-Na_2O-CaO glasses with closely similar compositions to those studied here [65, 66]. Limbach *et al.* [65] deconvoluted the full Raman spectrum for one such SiO_2-Na_2O-CaO glass, into several overlapping bands centred at 340, 460, 490, 540, 600, 630, 800, 950, 1080 and 1100 cm^{-1}. The bands at 490 cm^{-1} and 600 cm^{-1} were assigned [65] to the defect bands, D_1 and D_2 [48, 65] which correspond to oxygen breathing vibrations in 4- and 3-membered silica rings, respectively. The band at 540 cm^{-1} was assigned to delocalized Si–O–Si bridging oxygen vibrations [65] and the broad band at 460 cm^{-1} to symmetric Si–O–Si bridging oxygen vibrations [65]. The bands at 460, 540 and 800 cm^{-1} are clearly observed in our spectra for glasses Sb0 to Sb5 (Figure 5) and similar glasses in literature [65, 66].

The Raman band at 800 cm^{-1} is fundamental to spectra for pure SiO_2 glass and, as discussed earlier, and as summarised by Le Losq *et al.* [48], this band has been attributed to a number of origins. These include Si–O stretching involving oxygen motions in the Si–O–Si plane; the motion of the Si atom in its oxygen cage; and the threefold – degenerate “rigid cage” vibrational mode of TO_2 units. In the Raman spectrum for pure glassy SiO_2 this band can be fitted by two narrow, overlapping bands with energies corresponding to Si–O stretching vibrations [80, 81]. For the glasses studied here, the lack of spectral change at 800 cm^{-1} upon addition of (Sb_2O_3 + Al_2O_3), as shown in Figure 6, is perhaps more consistent with Si-O stretching modes / motion of the Si atom in its oxygen cage since (as discussed above) the (Si, Al)-O Q^n distribution appears to change in these glasses. However, other possible explanations for the origin of the 800 cm^{-1} band in the glasses studied here cannot be discounted.

The Raman spectra of the glasses undergo substantial changes in the lower-frequency region (200 – 800 cm^{-1}) upon incorporation of (Sb_2O_3 + Al_2O_3). As shown in Figures 5 and 6, these changes manifest as new bands at ~700 cm^{-1} and ~500 cm^{-1}, which (i) increase roughly proportionately in intensity to one another, and (ii) move to slightly lower Raman shifts, with increasing (Sb_2O_3 + Al_2O_3) contents. To first consider whether Al-bearing units may contribute to these bands, previous Raman studies of aluminosilicate [48, 63, 69] and aluminate [82] glasses deserve attention. Raman bands at ~500 - 600 cm^{-1} (aluminosilicate glasses [63, 69]) and at ~550 cm^{-1} and ~800 cm^{-1} (aluminate glasses [82]) have previously been observed, but with positions and linewidths that do not match those observed. However, progressive increase of the Al/Si ratio in SiO_2-Al_2O_3-Na_2O glasses [48] showed no evidence of a new band at ~700 cm^{-1} although changes near 500 cm^{-1} were observed. On balance, this suggests that Al-bearing units are less likely to be the primary source of the two new observed bands at ~700 cm^{-1} and ~500 cm^{-1} although contributions from Al-bearing units cannot be ruled out.

Raman bands related to Sb-O vibrational modes have very high intensities, as discussed by Miller *et al.* [73], who attributed this to a combination of (i) the glass-forming tendency of Sb_2O_3; (ii) the highly nonlinear geometry of the Sb-O-T (and Sb-O-Sb) bonding structures, and (iii) the high polarizability of the Sb-O bonds. Raman studies of Sb in antimonate [22, 23, 30, 32, 72, 73], borate [22, 31, 72], silicate [23, 74], aluminosilicate [74], germanate [73] and phosphate [26, 83] glasses have previously been published. An intense, broad Raman band centred at ~400-500 cm^{-1} has been widely observed and is attributed by a number of researchers [22, 23, 26, 72] to bending of trigonal pyramidal or pseudo-tetrahedral [:SbO_3] units. Terashima *et al.* [72] described this as an intense band near 450 cm^{-1} which can be divided into two peaks at 500 cm^{-1} and 440 cm^{-1}, which they assigned to the v_2 (symmetrical bending) and v_4 (asymmetrical bending) vibrational modes of SbO_3 units, respectively. Only a weak band near 700 cm^{-1} has been observed for pure v-Sb_2O_3 [73] as well as several other glasses [22, 24, 73, 74, 83]. This band has been attributed [26, 72] to symmetric stretching of [:SbO_3] units, although Mee *et al.* [23] assigned it to non-bridging oxygens (NBO's). Since here the intensity of these two bands increase roughly proportionately to each other (Figures 5 and 6), bending and stretching modes of [:SbO_3] units provide a more consistent explanation.

The local structure of Sb in these glasses was also studied for samples Sb5 and Sb10 by ^{121}Sb Mössbauer spectroscopy. The fitted parameters (Table 2) show that the large majority, approximately 90%, of the antimony is present in both glasses as Sb^{3+} [23, 24, 26, 30, 51-54] with the remainder as Sb^{5+} [23, 24, 51-54] As discussed in Section 3.2, there may be slight inaccuracy in the estimation of the relative proportions of Sb^{3+} and Sb^{5+} due to small differences between their recoil-free fractions, *f*. The large value of e^2Qq for Sb^{3+} confirms the highly asymmetric electric field distribution around the [:SbO_3] trigonal pyramids. Conversely, the second component, Sb^{5+} (present in SbO_6 units) has an isotropic electron distribution around the nucleus and hence the absence of quadrupole interaction for Sb^{5+} in the fits (see Section 3.2). Fitted centre shifts, δ, here given relative to the InSb standard to enable comparison with literature values (Table 2) are comparable to values obtained for Sb^{3+} and Sb^{5+} in SiO_2-Sb_2O_3 [23, 51], B_2O_3-Sb_2O_3 [24, 51], P_2O_5-Sb_2O_3 [26, 51] and Sb_2O_3-$ZnCl_2$ [30] glasses. The fitted δ and e^2Qq components for Sb^{3+}, and δ for Sb^{5+}, (Table 2) are consistent with the values for valentinite (Sb_2O_3) and crystalline Sb_2O_5 [23, 24, 52, 53]. As also noted previously [23, 24] this similarity in fitted parameters confirms the similarity in local environments of Sb^{3+} and Sb^{5+} in the glasses to their respective local environments in the corresponding crystalline materials. This conclusion is further supported by neutron diffraction of SiO_2-Sb_2O_3 glasses [22] and X-ray absorption spectroscopy of a wide range of Sb_2O_3 - (SiO_2,B_2O_3,GeO_2,As_2O_3) glasses [84-86], which confirmed consistent Sb–O coordination numbers of ~3, with Sb–O bond distances of 1.94–1.97 Å that are largely independent of glass composition; with Sb^{3+} in trigonal pyramidal coordination and Sb^{5+} in octahedral coordination.

The strong fluxing effect of Sb_2O_3 during melting of the glasses studied (see Section 4.1), and the evidence from Raman spectroscopy discussed earlier in this Section, are internally consistent and indicate a strong depolymerising effect of Sb_2O_3 on the (alumino)silicate network. This, in turn, suggests the presence of (Si, Al)-O-Sb bonds, with Sb providing NBO's. A number of workers have investigated structural effects of Sb on silicate and borate glass networks using ^{29}Si MAS-NMR [23, 28], ^{11}B MAS-NMR [24, 28, 72, 84], ^{27}Al MAS-NMR [28] and X-ray absorption spectroscopy (XAS) [83, 84]. On the basis of XAS, Ellison and Sen [83] concluded that the geometry of the SbO_3 coordination polyhedra is extremely well-constrained from one glass family to another, and Sb^{3+} behaves as a classic network former (NWF) cation in binary oxide glasses, creating a continuous random network of Sb-O-M bonds where M = Sb, As, Ge, Si, or B depending on the glass system. For silicate glasses, Mee *et al.* [23] showed a strong depolymerising effect of Sb_2O_3 on binary SiO_2-Sb_2O_3 glasses using ^{29}Si MAS-NMR, assuming that 2 NBO are formed for each Sb_2O_3 molecule, where NBO are Si–O–Sb oxygen links with significant covalence in the bonding. Terashima *et al.* [72], Holland *et al.* [24] and Youngman *et al.* [84] all found evidence for B-O-Sb linkages in binary B_2O_3-Sb_2O_3 glasses using ^{11}B MAS-NMR. However, Wood *et al.* [28], who studied SiO_2-B_2O_3-Al_2O_3-CaO-Sb_2O_3 glasses containing 0 to 5.5 mol% Sb_2O_3 (thereby more similar to those glasses studied here) using multiple MAS-NMR isotopes, found a more complex situation where, regardless of the deconvolution method they used, addition of Sb_2O_3 appeared to increase Si Q^n for Sb_2O_3 contents of 0 to 1.5 mol%, above which the Q^3/Q^4 ratio remained approximately constant. From ^{27}Al MAS-NMR, the Al remained consistently 4-coordinated for all glasses, and from ^{11}B MAS-NMR the $^{[4]}B^{3+}/^{[3]}B^{3+}$ ratio increased from 0.45 in the Sb-free glass to 0.65 at 3 mol% Sb_2O_3, above which it remained approximately constant [28]. However, Wood *et al.* noted that from 0 to 1.5 mol% Sb_2O_3, the glasses exhibited visible opalization and, from a TEM study, attributed this to iron nanoparticles. They concluded that Sb^{3+} was most likely present in their glasses as a combination of trigonal pyramids forming Si-O-Sb bonds and tetrahedral $(SbO_4)^-$ units requiring charge balance from the Ca^{2+} cations. In light of our evidence from thermal properties, and from Raman and ^{121}Sb Mössbauer spectroscopies, results for the glasses studied here are more consistent with the majority view that Sb^{3+} exists as trigonal pyramid (:SbO_3) units, introducing multiple NBO's and forming Si-O-Sb linkages, thereby decreasing the average Si Q^n.

4.3. Redox

The redox behaviour of Sb in oxide glasses has been widely studied, partly due to its efficacy and employment over many years as a refining agent in glass manufacturing (see Section 1). Here, the areas of the fitted components for Sb^{3+} and Sb^{5+} in glasses Sb5 and Sb10 have been confirmed by ^{121}Sb Mössbauer spectroscopy to be approximately 90% Sb^{3+}, with the balance Sb^{5+} (Table 2). However, as discussed in Section 3.2, it is possible that $f(Sb^{3+}) / f(Sb^{5+})$ deviates slightly from a value of 1 and hence the extracted $Sb^{3+}/\Sigma Sb$ ratios may be slightly different than ~0.9. Within uncertainties, the area ratios and hence the $Sb^{3+}/\Sigma Sb$ ratios are the same for both glasses. These measured redox ratios are remarkably consistent with measured redox ratios for Sb in other silicate glasses melted at similar temperatures, including TV glasses [10, 11], SiO_2-Sb_2O_3 glasses [23], borosilicate glasses [87] and SiO_2-Na_2O-CaO glasses [6, 14]. Redox data for multiple silicate and borosilicate glasses melted in air at temperatures broadly similar to the melting temperature used here thus shows that $Sb^{3+}/\Sigma Sb$ is consistently ~0.80 - 0.95, from low Sb_2O_3 contents of less than 1 mol% [6, 10, 11, 14] to high (>10 mol%) contents [23, 87], and this behaviour is consistent with measured Sb redox potentials in oxide glasses [20, 21]. It is established that glass composition can also play a significant role in determining redox ratios such as $Sb^{3+}/\Sigma Sb$ [13, 14, 86, 88], and this behaviour can be described by accepted glass redox models for composition - structure – basicity relations [13, 14, 20, 21, 42, 86, 88-91].

The oxidising effects of the Sb_2O_3 batch additions are also manifested in UV-Vis-nIR optical absorption spectra (Figure 3). The Sb0 antimony-free glass manifested very weak absorption peaks (Figure 3, inset) attributed to Fe^{2+} and Fe^{3+}. XRF (Table 1) confirmed the presence of impurity levels of Fe_2O_3 in these glasses, probably arising from impurities in the raw materials used. However, this provides a useful fingerprint for glass redox and for any mutual redox interactions involving Fe and Sb. The observed absorption bands for glass Sb0, marked in the Figure 3 inset, include a broad band centred at ~10,500 cm^{-1} which is widely attributed to octahedrally-coordinated Fe^{2+} [5, 8, 16-19] and narrower bands centred at 22,600 cm^{-1}, 23,800 cm^{-1} and 26,500 cm^{-1}, all attributed to tetrahedrally- and octahedrally- coordinated Fe^{3+} [5, 8, 17-19]. Addition of Sb_2O_3 to the glass, at all levels studied, oxidised the Fe^{2+} to Fe^{3+}, according to equation (3), consistent with literature [5, 7-10, 15, 20, 21] and demonstrated by the disappearance of the Fe^{2+} absorption band centred at ~10,500 cm^{-1}. Similar results were recently published for Sb_2O_3-doped borosilicate glasses with trace levels of impurity Fe_2O_3 by Singkiburin *et al.* [7], who showed the disappearance of the Fe^{2+} band and near-complete oxidation of Fe^{2+} to Fe^{3+} at Sb_2O_3 doping levels between 0.10 and 0.50 mol%.

The final redox-active element present in the glasses studied here is sulphur. As discussed in Section 4.2, the Raman band at ~990 cm^{-1} is due to ν_1 symmetric S-O stretching modes in SO_4^{2-} units. No other Raman bands were observed, including the weak O-S-O bending and stretching modes in SO_4^{2-} units [78, 79] but given the low sulphate contents of all glasses this is not unexpected. No Raman bands that would indicate the presence of lower oxidation states of sulphur [75, 76] were observed, and redox potentials [20, 21] confirmed that the only expected oxidation state of sulphur in glasses prepared under oxidising melting conditions, such as those used here, is S(VI). The disappearance of SO_3 from the glass with increasing (Sb_2O_3 + Al_2O_3) content (Table 1) may be related to accelerated transport properties due to the lower melt viscosities that the Sb_2O_3 additions enable, however, this does not explain the complete disappearance of sulphate with higher (Sb_2O_3 + Al_2O_3) additions and suggests (an)other mechanism(s). Sulphate is evolved as SO_2 gas during glass melting, thereby decreasing the amount of dissolved SO_4^{2-} species with increasing melting time [45, 78] yet such changes are slow and rarely lead to the complete loss of sulphate. Recent XRF analysis of sulphate content of fused beads of soda-lime-silica glass and feldspar Certified Reference Materials (CRM's) using the same XRF equipment and program used here [45] confirms that the observed sulphate loss is real and quantified, and is not related to errors or uncertainties of measurement. Changes in sulphate solubility of the glass melt as a result of compositional change [76-79] may be one possible explanation, and such effects have been widely reported [76-79, 90]. As illustrated by Backnaes and Deubener [90] in their consideration of a wide body of literature, the solubility of sulphate in high-Al_2O_3 silicate glasses can be up to an order of magnitude lower than in SiO_2-Na_2O-CaO glasses. This may suggest that the increased Al_2O_3 that accompanies increasing Sb_2O_3 in our glasses may also contribute to the observed decreases in analysed SO_3 content. Sulphate evolution from oxide glass melts can be accurately described by a simple diffusion-based model [4, 45]. However, from XRF data (Table 1) it is clear that even at 1 mol% Sb_2O_3 addition the SO_3 content of glass Sb1 is barely over half that of the Sb0 antimony-free glass, with only a small increase in Al_2O_3 content from 0.76 to 1.18 mol%, suggesting rapid diffusion, perhaps facilitated by lower melt viscosities. Hence the increased Al_2O_3 content is unlikely to be solely responsible for the loss of SO_3. The effects of Sb_2O_3 on SO_3 retention are less clear, but evidence from archaeological studies [8, 92, 93] shows that many ancient soda-lime-silica type glasses exhibit SO_3 and Sb_2O_3 contents of up to a few weight %. Moreover, a loose linear correlation between SO_3 and Sb_2O_3 contents has been observed [92, 93] for up to ~1 weight % (approximately 0.75 mol%) SO_3 and up to ~8 weight % (approximately 2 mol%) Sb_2O_3. Clearly, therefore, the behaviour of the glasses studied here differed from the behaviour observed in the ancient glasses [8, 92, 93] and this suggests that the Sb_2O_3 additions are not solely responsible for the loss of SO_3. Other potential factors for consideration include mutual redox interactions between sulphur and antimony species. These are unlikely because any reduction of S^{6+} species to a lower oxidation state through a mutual redox reaction with Sb^{3+} is precluded by redox potentials [20, 21] wherein if any reaction between Sb and S did take place, it would be to reduce Sb^{5+} to Sb^{3+} and oxidise S^{2-} to S^{6+}. However, since we have established that the sulphur is present in all glasses solely in its fully-oxidised S^{6+} form (see above and Section 4.2) and little Sb^{5+} exists in these glasses, this reaction would not be possible. The observed oxidation of Fe^{2+} to Fe^{3+} (Figure 3 inset), consistent with equation (3), and the absence of any Raman bands characteristic of lower oxidation states of sulphur (Figures 5 and 6), as discussed above, support this conclusion. Finally, the previously discussed studies of ancient soda-lime-silica type glasses [8, 92, 93] show that Sb and S species can coexist in such glasses. The specific effects of (Sb_2O_3 + Al_2O_3) on SO_3 solubility and retention, and their mutual interactions in silicate glasses have not, to our knowledge, been studied previously and further research is thus required to more fully understand the observed behaviour.

Thermogravimetric analysis (TGA), shown in Figure 8, illustrates a clear trend in weight gain from 700°C to 1175°C, with weight loss occurring at temperatures above 1175°C. This weight gain displays a linear relationship with analysed Sb_2O_3 content (Figure 9), enabling it to be attributed to oxidation of Sb^{3+} (Sb_2O_3) to Sb^{5+} (Sb_2O_5) through reaction with atmospheric oxygen (5).

$$Sb_2O_3 + O_2 \rightarrow Sb_2O_5 \qquad (5)$$

At temperatures above 1175°C this reaction reverses and Sb^{5+} begins to reduce to Sb^{3+}, releasing O_2 (2) as evidenced by the corresponding weight loss. This temperature is consistent with de Best [89] and Kim *et al.* [94], who showed that 1150-1200°C corresponds with the onset temperature for an increase in oxygen equilibrium pressure for TV glasses, which are alkali-alkaline earth silicate glasses and are thus broadly similar to the soda-lime-silica glasses studied here.

Krol and Rommers [10] studied the $Sb^{3+}/\Sigma Sb$ redox ratio in TV glasses and compared glasses prepared from batch materials with those prepared from remelted cullet. For their remelted cullet samples (thus more comparable to our TGA samples), their $Sb^{3+}/\Sigma Sb$ ratios remained > 0.9 for glasses melted at all temperatures studied (900°C to 1500°C). However, within this narrow redox range, the $Sb^{3+}/\Sigma Sb$ redox ratio did slightly vary with melting temperature, decreasing from 900°C to 1200°C and then increasing again from 1200°C to 1500°C, with the minimum value of $Sb^{3+}/\Sigma Sb$ occurring at 1200°C.

This is again qualitatively consistent with our TGA results, i.e. maximum Sb oxidation occurring at ~ 1200°C. Krol and Rommers [10] concluded that Sb^{3+}/Sb^{5+} equilibration is governed by two processes – one relatively fast, where equilibrium is attained with oxygen in the melt; and one relatively slow, where the melt reaches equilibrium with the surrounding atmosphere. They obtained a diffusion length of 0.04 cm after 200 hours' melting at 1200°C, calculating the diffusion coefficient $D = 2.7 \times 10^{-9}$ cm^2 s^{-1}. Closely similar diffusion coefficients were also obtained by Kim and Lee [11]. Considering that Krol and Rommers [10] studied glass melts of 1 cm^3 (~2.5 to 3 g glass) whilst our TGA samples were ~30 mg (thus having far greater surface area / volume ratios with a far smaller sample) the two sets of results are not inconsistent. Research by Lee *et al.* [12] using a Raman microprobe to study O_2 dissolution from bubbles in doped SiO_2-Na_2O-CaO glasses when reheated to 1000°C, indicated that for the glasses doped with Sb_2O_3 the reaction shown here in equation (5) proceeded particularly rapidly, with most of the O_2 within the bubbles dissolving within the glass after only 10 minutes. Those timescales are of the same order of magnitude as those observed here from TGA, and the origins of the apparent differences in oxidation rate with Krol and Rommers [10] are likely to derive from the large differences in sample surface area / volume ratios of the respective glass melts.

Our TGA experiments were conducted at a heating rate of 10°C min^{-1}, hence the time to reach 1175°C from 700°C, when the weight gain began, was 47.5 minutes. This indicates rapid melt / atmospheric O_2 reaction. Similarly rapid reactions, with even greater levels of O_2 uptake, were reported by de Laune *et al.* [54] for $FeSb_2O_4$. From Figure 9 it was established that the observed behaviour is consistent with equation (5) above, and hence we can estimate the equilibrium $Sb^{3+}/\Sigma Sb$ ratio for our glasses at any temperature between 700°C and 1200°C, if volatilisation and other interactions are neglected. Taking glass Sb10 as an example, and assuming that $Sb^{3+}/\Sigma Sb$ in the TGA sample at 700°C is the same as at 20°C (293 K), we have established by ^{121}Sb Mössbauer spectroscopy that $Sb^{3+}/\Sigma Sb$ ~0.9. This corresponds to 33.35 weight % Sb_2O_3 and 3.71 weight % Sb_2O_5 equivalent in glass Sb10 at 700°C. Heating from 700°C to 1175°C produces a weight gain of 1.86 weight % (Figure 8). If all Sb^{3+} in the glass were fully oxidised to Sb^{5+}, this would produce a weight gain of 3.66 weight %. Hence 1.86 / 3.66 ≈ 50 %, thus half of all Sb^{3+} has been oxidised to Sb^{5+} when 1175°C is reached in the TGA experiments, i.e. $Sb^{3+}/\Sigma Sb \approx (0.5 \times 0.9) \approx 0.45$ at 1175°C. Since the established relationship applies to all studied Sb_2O_3 contents, is linear, and passes close to the origin (Figure 9), this estimation applies to all Sb_2O_3 contents studied. This behaviour is consistent with the results of voltammetric studies by Yoshida *et al.* [14] and Yamashita *et al.* [95], who showed, for SiO_2-Na_2O-CaO glasses that the equilibrium $Sb^{3+}/\Sigma Sb$ ratio at 1200°C was ~0.5. In addition, Yamashita *et al.* [95] also showed that the rate of evolved and removed O_2 gas quantities (i.e. when $[Sb^{3+}] = [Sb^{5+}]$) was at its maximum at 1200°C, again consistent with our TGA results which show this maximum at 1175°C. The glass melts of Yoshida *et al.* [14] and Yamashita *et al.* [95] were equilibrated in air for 11 hours at 1400°C and 95 hours at 1200°C, respectively, before they carried out their measurements in order to ensure that redox equilibrium had been achieved. They did not state the mass of glass melted, but given the experimental setups described [14, 95], it can be reasonably estimated that at least 10-100 g and possibly more glass (and thus high volumes with much lower surface area / volume ratios than our TGA samples) was melted, thus explaining the need for longer redox equilibration times. By comparison, 200 g of each of our glasses were melted in air for 5 hours at 1450°C then very small (~30 mg) samples of each glass were powdered and then heated at 10°C min^{-1} during the TGA experiments. In light of the results of Yoshida *et al.* [14] and Yamashita *et al.* [95], our TGA results are thus consistent with achieving, or at least approaching, Sb redox equilibrium dynamically during the TGA experiments. This is because the $Sb^{3+}/\Sigma Sb$ redox ratio of ~0.9, achieved here during glass melting at 1450°C, was essentially frozen-in to the TGA samples prior to the TGA experiments and consequently the $Sb^{3+}/\Sigma Sb$ redox ratio in the TGA samples that was not at equilibrium for temperatures lower than 1450°C. Thus, as the TGA samples were heated from 20°C upwards, the $Sb^{3+}/\Sigma Sb$ ratio would have decreased at temperatures above T_g (capturing oxygen and thereby increasing sample weight), with the $Sb^{3+}/\Sigma Sb$ ratio decreasing towards the equilibrium value for that temperature. However, the TGA experiments were dynamic processes, thus the $Sb^{3+}/\Sigma Sb$ ratio continued to decrease until the sample reached a temperature (1175°C) where it had achieved the equilibrium $Sb^{3+}/\Sigma Sb$ ratio for that temperature (~0.5, as discussed above), and as temperature increased further above 1175°C, the $Sb^{3+}/\Sigma Sb$ ratio thus began to increase accordingly. This behaviour provides evidence that antimony redox equilibration during the TGA experiments was particularly rapid, and it illustrates that using TGA-sized crucibles and small (mg) sample sizes can provide a practical route for rapid access to redox equilibrium in glass melts containing Sb and, potentially, other multivalent cations.

4.4. Optical Properties

UV-Vis-nIR absorption spectra (Figure 3) show changes in the oxidation state of the Fe impurities according to equation (3), as discussed in Section 4.3. However, the UV-Vis-nIR spectra also show a characteristic red-shift of the UV absorption edge as a function of Sb_2O_3 content, of the order of 4500 cm^{-1} between sample Sb0 and Sb10. This is consistent with increasing yellow colouration of the glasses due to absorption of a proportion of violet and blue light by the tail of the UV edge. Comparable levels of visible colouration were also obtained by Singkiburin *et al.* [7], who added up to 2 mol% Sb_2O_3 to borosilicate glasses. Red-shift of the UV edge energy due to Sb incorporation has also been observed by many other researchers [7, 25, 31, 35, 37, 39, 41, 74, 96, 97]. This red-shift and the resulting yellow-gold colouration of the glass is caused by the presence of intense absorption bands centred in the far-UV which produce tails that absorb at visible energies. These absorption bands arise from the spin-forbidden $^1S_0 \rightarrow {}^3P_1$ transition of Sb^{3+} (centred at 40,000 - 46,000 cm^{-1}) [36-42, 97] and the Laporte-allowed electron-transfer band [42] of Sb^{5+} (centred at > 50,000 cm^{-1}) [38, 39, 42]. Strong UV absorption bands causing visible yellow-gold colouration are typical of oxide glasses containing substantial levels of 5p- or 6p- ns^2 outer electron configuration ions which exhibit s→p transitions (e.g. Pb^{2+}, Bi^{3+}, Sb^{3+}) [25, 31-34, 36-42, 96, 97]. The red-shift of the UV edge here (Figure 3) between samples Sb0 and Sb10 is ~4,500 cm^{-1}, with smaller shifts for lower Sb additions. This effect is accompanied by reduced visible colouration due to the oxidation of Fe^{2+} impurities to Fe^{3+}, as discussion in Section 4.3. The iron impurities also contribute broad oxygen-metal charge transfer (OMCT) absorption bands centred in the far-UV [17, 19, 36, 38]. For soda-lime-silica and borosilicate glasses these broad bands are centred at ~39,500 cm^{-1} (Fe^{3+}) and ~46,500 cm^{-1} (Fe^{2+}) [19, 38] but given the low (≤ 0.01 mol%) measured Fe_2O_3 contents of our glasses (Table 1), the spectral contribution here, in the energy range of interest, from the tails of these OMCT bands is very small compared with the effects of the tails from the far-UV Sb^{3+} and Sb^{5+} bands.

Consideration of the electronic bandgaps for the corresponding antimony oxides, as obtained by Allen *et al.* [97], shows energies of ~22,000 to ~28,550 cm^{-1} for α-, β- and γ- forms of Sb_2O_3, and ~6,130 cm^{-1} for Sb_2O_5. This is consistent with the observed shifts in UV-edge position observed in this study with increasing Sb_2O_3 content, assuming no changes in the $Sb^{3+}/\Sigma Sb$ ratio which is supported by our ^{121}Sb Mössbauer spectroscopy measurements of the Sb5 and Sb10 glasses. These bandgap energies, particularly of Sb_2O_5, are also consistent with the nonlinear visible and near-IR absorption observed for the higher-Sb glasses studied here (Figure 3), and particularly glass Sb10. It would be interesting to study the effects on UV edge position in oxide glasses with considerably different $Sb^{3+}/\Sigma Sb$ redox ratios, in the context of bandgap energies of the corresponding oxides, and further research on this topic is planned.

A single broadband luminescence band, centred at the edge of the visible-range energies (25,200 – 25,600 cm^{-1}), was obtained at all Sb_2O_3 contents (Figure 4) when excited by 40,000 cm^{-1} UV radiation. The strongest luminescence was obtained at the lowest Sb_2O_3 content studied, 0.5 mol%, with lower intensities at 1 and 5 mol% Sb_2O_3, then yet lower intensity at 10 mol% Sb_2O_3. This behaviour indicates luminescence quenching, with the maximum achievable intensity in this glass system shown to be < 1 mol% Sb_2O_3. Further research is required to establish the optimal Sb_2O_3 content, and also to assess luminescence lifetimes. These have previously been measured in borate and phosphate glasses [40, 41]. Reisfeld *et al.* [40] observed two distinct lifetimes, of 67 ns and 2.0 μs (P_2O_5-Na_2O glass) and 93 ns and 2.3 μs (B_2O_3-Na_2O glass) and provided a detailed rationale that explained their observed deviation from an exponential function of the luminescence decay curve at room temperature. Masai *et al.* [41] studied B_2O_3-ZnO glasses and also observed two distinct lifetimes, with one in the nanosecond range and one of 3.6 μs. The single broad emission band is attributed to the spin-forbidden $^3P_1 \rightarrow {}^1S_0$ transition of Sb^{3+} [40, 41, 98] and its width leads to emission across a range of visible energies, only reaching 10% of its peak intensity at 18,000 cm^{-1} (Figure 4).

As noted in Section 1, the combination of enhanced UV absorption and re-emission of absorbed energy as lower-energy (visible) photons could have particular advantages in some solar energy applications [43, 44, 99]. For example, such glass could simultaneously: (i) provide enhanced UV protection for polymeric and photovoltaic components of solar energy modules without doping the cover glass with transition metals, lanthanides or other constituents that would produce visible and / or near-IR absorption bands which would reduce the number of photons reaching the solar cell and thereby decreasing its efficiency [43, 44, 99]; and (ii) increase the efficiency of commercial solar cell materials by converting UV photons to visible photons, thereby providing additional photons with energies capable of being efficiently absorbed by the solar cell and converted to electrical current [43, 44, 99]. This performance-enhancing behaviour has recently been studied for several d^0-configuration *d*-block cations [43] and for the ns^2 cation, Bi^{3+} [44]; and for TiO_2 and ZnO coated soda-lime-silica float glasses [99]. On a related theme, Xu *et al.* [98] noted that the main absorption of chlorophyll matches the blue Sb^{3+} emission, suggesting that glasses doped with Sb^{3+} ions could potentially be used to convert UV light into blue light to promote plant photosynthesis. Additions of Sb_2O_3 to low-cost commercial float-type soda-lime-silica glasses could thus enable new lower melting energy glasses, solar energy glasses, or novel glasses utilising the beneficial thermal or optical properties of Sb_2O_3 additions.

5. Conclusions

Float glass-type SiO_2-Na_2O-CaO glasses with Sb_2O_3 contents of 0 to 10 mol% were X-ray amorphous; and increasing additions of Sb_2O_3 resulted in progressive decreases in glass transition temperature (T_g) and dilatometric softening point (T_d), despite increases in Al_2O_3 content from higher crucible corrosion during melting. These data, combined with viscosity modelling and Raman spectroscopy, confirmed the very strong fluxing action of Sb_2O_3 in silicate glasses, assisted by the decrease in average (Si, Al)-O Q^n speciation that it enables, indicating that Sb_2O_3 additions could be a method of melting energy reduction in glasses where the toxicity of Sb is acceptable. Antimony was shown by ^{121}Sb Mössbauer spectroscopy to be incorporated as Sb^{3+} ($Sb^{3+}/\Sigma Sb \approx 0.9$) with Sb present as trigonal pyramidal [:SbO_3] polyhedral and Sb^{5+} in octahedral coordination. Sulphate content decreased with increasing Sb_2O_3 content, reaching zero at 10 mol% Sb_2O_3, with the exact mechanism unclear, but which may be related to the strong decreases in melt viscosity enabled by Sb_2O_3 incorporation. TGA experiments showed oxidation then reduction of antimony, with oxidation ($Sb^{3+} \rightarrow Sb^{5+}$) at 700°C – 1175°C and reduction ($Sb^{5+} \rightarrow Sb^{3+}$) > 1175°C, with rapid redox equilibration enabled by the small TGA sample size. Optical absorption spectroscopy showed the UV absorption edge shifting to lower wavenumbers with increasing Sb_2O_3 content, consistent with increasing intensity of far-UV absorption bands arising from Sb^{3+} and Sb^{5+} $s \rightarrow p$

transitions. UV-Vis-nIR fluorescence spectroscopy evidenced a broad luminescence band due to the spin-forbidden $^3P_1 \rightarrow {}^1S_0$ transition of Sb^{3+}, centred at ~25,000 cm^{-1} and Stokes shifted from the $^1S_0 \rightarrow {}^3P_1$ absorption transition of Sb^{3+} at ~40,000 cm^{-1}. The strongest emission occurred for 0.5 mol% Sb_2O_3, with concentration quenching reducing intensities at higher Sb_2O_3 contents. Additions of Sb_2O_3 to low-cost commercial float-type soda-lime-silica glasses could thus prove beneficial in enabling lower melting energy glasses, new solar energy glasses or new glasses for other, related applications.

Acknowledgements

T-YC, GG, HS, RJD and PAB acknowledge with thanks funding support from the UK Engineering and Physical Science Research Council (EPSRC) under Grant EP/R020957/1, New Industrial Systems: Manufacturing Immortality. The authors also thank Frank J. Berry for useful discussions.

References

[1] F. T. Wallenberger and P. A. Bingham, Fiberglass and glass technology: energy-friendly compositions and applications, Springer, New York, 2010, 474 pp.

[2] J. E. Shelby, Introduction to glass science and technology, 2nd Ed., Royal Society of Chemistry, London, 2005.

[3] M. Hujová and M. Vernerová, Influence of fining agents on glass melting: a review, part 1. Ceramics –Silikaty 61 (2017) 119–126.

[4] M. Hujová and M. Vernerová, Influence of fining agents on glass melting: a review, part 2. Ceramics –Silikaty 61 (2017) 202-208.

[5] W. A. Weyl, Coloured glasses, Society of Glass Technology, Sheffield, 1951.

[6] M. Cable and A. A. Naqvi, The refining of a soda-lime-silica glass with antimony, Glass Technology 16 (1975) 2-11.

[7] N. Singkiburin, N. Srisittipokakun and J. Keawkhao, Effect of antimony (III) oxide on reduction of bubbles from glass melting process, Journal of Physics: Conference Series 1428 (2020) 012030.

[8] P. A. Bingham and C. M. Jackson, Roman blue-green bottle glass: chemical-optical analysis and high temperature viscosity modelling, Journal of Archaeological Sciences 35 (2008) 302-309.

[9] A. B. Atkarskaya and V. N. Bykov, Clarification of glass using arsenic and antimony oxides, Glass and Ceramics 60 (2003) 389-391.

[10] D. M. Krol and P. J. Rommers, Oxidation-reduction behaviour of antimony in silicate glasses prepared from raw materials and cullet, Glass Technology 25 (1984) 115-118.

[11] K.-D. Kim and S.-H. Lee, Redox behaviour and diffusivity of antimony and cerium ions in alkali alkaline earth silicate glass melts, Ceramics – Silikáty 54 (2010) 14-18.

[12] S. W. Lee, K. S. Hong and R. A. Condrate Sr., Raman microprobe investigation of oxygen and carbon dioxide dissolution from bubbles in silicate glasses containing antimony oxide, Journal of Materials Science 26 (1991) 4250-4254.

[13] M. Yokozeki, T. Moriyasu, H. Yamashita and T. Maekawa, Electrochemical studies of the redox behavior of antimony ions in sodium borate and silicate melts, Journal of Non-Crystalline Solids 202 (1996) 241-247.

[14] S. Yoshida, T. Sudo, M. Kato, T. Sugawara, J. Matsuoka, Y. Miura and Y. Kii, Effects of composition on redox behaviors of antimony or arsenic ion in silicate melts by differential pulse voltammetry, Journal of Non-Crystalline Solids 356 (2010) 2842-2849.

[15] A.-I. Bidegaray, A. Ceglia, M. R. Cicconi, V.-T. Pham, A. Crabbé, E. A. Mernissi Cherigui, K. Nys, H. Terryn, D. R. Neuville and S. Godet, An in-situ XANES investigation of the interactions between iron, manganese and antimony in silicate melts, Journal of Non-Crystalline Solids 502 (2018) 227-235.

[16] M. Hubert, A. J. Faber, H. Sesigur, F. Akmaz, S. R. Kahl, E. Alejandro and T. Maehara, Impact of redox in industrial glass melting and importance of redox control, 77th Conference on Glass Problems: Ceramic Engineering and Science Proceedings, Editor: S.K. Sundaram, Wiley, New York, pp. 115-129.

[17] R. G. Burns, Mineralogical applications of crystal field theory, Cambridge University Press, Cambridge, 1993.

[18] P. A. Bingham, J. M. Parker, T. Searle, J. M. Williams, K. Fyles, Redox and clustering of iron in silicate glasses, Journal of Non-Crystalline Solids 253 (1999) 203-209.

[19] T. T. Volotinen, J. M. Parker and P. A. Bingham, Concentrations and site partitioning of Fe^{2+} and Fe^{3+} ions in a soda-lime-silica glass obtained by optical absorbance spectroscopy, Physics and Chemistry of Glasses: European Journal of Glass Science and Technology B 49 (2008) 258-270.

[20] H. D. Schreiber, Redox processes in glass-forming melts, Journal of Non-Crystalline Solids 84 (1986) 129-141.

[21] H. D. Schreiber, N. R. Wilk Jr. and C. W. Schreiber, A comprehensive electromotive force series of redox couples in soda-lime-silicate glass, Journal of Non-Crystalline Solids 253 (1999) 68-75.

[22] R. G. Orman, Characterisation of novel antimony (III) oxide-containing glasses, PhD thesis, University of Warwick, UK, 2010.

[23] M. Mee, B. C. Davies, R. G. Orman, M. F. Thomas and D. Holland, Antimony and silicon environments in antimony silicate glasses, Journal of Solid State Chemistry 183 (2010) 1925-1934.

[24] D. Holland, A. C. Hannon, M. E. Smith, C. E. Johnson, M. F. Thomas and A. M. Beesley, The role of Sb^{5+} in the structure of Sb_2O_3–B_2O_3 binary glasses—an NMR and Mössbauer spectroscopy study, Solid State Nuclear Magnetic Resonance 26 (2004) 172-179.

[25] S. Y. Marzouk and F. H. El-Batal, Infrared and UV–visible spectroscopic studies of gamma-irradiated Sb_2O_3–B_2O_3 glasses, Journal of Molecular Structure 1063 (2014) 328-335.

[26] M. Nalin, Y. Messaddeq, S. J. L. Ribeiro, M. Poulain, V. Briois, G. Brunklaus, C. Rosenhahn, B. D. Mosel and H. Eckert, Structural organization and thermal properties of the Sb_2O_3–$SbPO_4$ glass system, Journal of Materials Chemistry 14 (2004) 3398-3405.

[27] M. Nalin, M. Poulain, M. Poulain, S. J. L. Ribeiro and Y. Messaddeq, Antimony oxide based glasses, Journal of Non-Crystalline Solids 284 (2001) 110–116.

[28] J. G. Wood, S. Prabakar, K. T. Mueller and C. G. Pantano, The effects of antimony oxide on the structure of alkaline-earth alumino borosilicate glasses, Journal of Non-Crystalline Solids 349 (2004) 276–284.

[29] D. F. Franco, E. E. Carvajal, J. P. Donoso, M. A.P. Silva, A. C. Sant'Ana, H. Fares, C. J. Magon and M. Nalin, Structural and EPR studies of Cu^{2+} ions in $NaPO_3$ – Sb_2O_3 – CuO glasses Journal of Non-Crystalline Solids 503 (2019) 169–175.

[30] J. A. Johnson, D. Holland, J. Bland, C. E. Johnson and M. F. Thomas, Cation coordination in oxychloride glass, Journal of Physics: Condensed Matter 15 (2003) 755–764.

[31] G. Jagannath, B. Eraiah, A. Gaddam, H. Fernandes, D. Brazete, K. Jayanthi, K. N. Krishnakanth, S. V. Rao, J. M. F. Ferreira, K. Annapurna and A. R. Allu, Structural and femtosecond third-order nonlinear optical properties of sodium borate oxide glasses: effect of antimony, Journal of Physical Chemistry C 123 (2019) 5591-5602.

[32] K. Ouannes, K. Lebbou, B. M. Walsh, M. Poulain, G. Alombert-Goget and Y. Guyot, New Er^{3+} doped antimony oxide based glasses: thermal analysis, structural and spectral properties, Journal of Alloys and Compounds 649 (2015) 564-572.

[33] T. Som and B. Karmakar, Green and red fluorescence upconversion in neodymium-doped low phonon antimony glasses, Journal of Alloys and Compounds 476 (2009) 383–389.

[34] K. Ouannes, K. Lebbou, B. M. Walsh, M. Poulain, G. Alombert-Goget and Y. Guyot, Antimony oxide based glasses, novel laser materials. Optical Materials 65 (2017) 8-14.

[35] X. Heng, Q. Qian, X. Chen, L. Liu, X. Zhao, D. Chen and Z. Yang, Reduced radiation damage in a multicomponent phosphate glass by Nb^{5+} or Sb^{3+} doping, Optical Materials Express 5 (2015) 2272-2280.

[36] D. Möncke and D. Ehrt, Photoionization of polyvalent ions, in: Materials Science Research Horizons, Editor: H. P. Glick, Nova Science Publishers, New York (2007) pp. 1-56.

[37] D. Möncke and D. Ehrt, Photoionization of As, Sb, Sn, and Pb in metaphosphate glasses. Journal of Non-Crystalline Solids 345-346 (2004) 319–322.

[38] D. Ehrt and P. Eberling, Radiation defects in borosilicate glasses, Glass Technology 44 (2003) 46-49.

[39] A. M. Efimov, A. I. Ignatiev, N. V. Nikonorov, and E. S. Postnikov, Photo-thermo-refractive glasses: effects of dopants on their ultraviolet absorption spectra, International Journal of Applied Glass Science 6 (2015) 109-127.

[40] R. Reisfeld, L. Boehm and B. Barnett, Luminescence and Nonradiative Relaxation of Pb^{2+}, Sn^{2+}, Sb^{3+}, and Bi^{3+} in Oxide Glasses, Journal of Luminescence 15 (1975) 140-150.

[41] H. Masai and T. Yanagida, Photoluminescence of ns^2-type center-containing zinc borate glasses, Journal of Non-Crystalline Solids 431 (2016) 83–87.

[42] J. A. Duffy, Prediction of ultraviolet absorption spectra of p-block ions in oxide media possible application to redox equilibria in glasses and molten salts, Journal of the Chemical Society, Faraday Transactions 2: Molecular and Chemical Physics 74 (1978) 1504-1514.

[43] B. L. Allsopp, G. Christopoulou, A. Brookfield, S. D. Forder and P. A. Bingham, Optical and structural properties of d^0 ion-doped silicate glasses for photovoltaic applications, Physics and Chemistry of Glasses: European Journal of Glass Science and Technology Part B 59 (2018) 193-202.

[44] B. L. Allsopp, R. Orman, S. R. Johnson, I. Baistow, G. Sanderson, P. Sundberg, C. Stålhandske, L. Grund, A. Andersson, J. Booth, P. A. Bingham and S. Karlsson, Towards thinner cover glasses for photovoltaic devices with enhanced service lifetimes and lifetime efficiencies, Progress in Photovoltaics: Research and Applications (under review, February 2020).

[45] A. M. T. Bell, D. J. Backhouse, W. Deng, J. D. Eales, E. Kilinc, K. Love, P. Rautiyal, J. C. Rigby, A. H. Stone, S. Vaishnav, G. Wie-Addo and P. A. Bingham, X-ray fluorescence analysis of feldspars and silicate glass: effects of melting time on fused bead consistency and volatilization, Minerals 10 (2020) 442.

[46] A. Fluegel, http://glassproperties.com/, accessed 20/05/2020.

[47] D. R. Neuville and B. O. Mysen, Role of aluminium in the silicate network: in situ, high-temperature study of glasses and melts on the join SiO_2-$NaAlO_2$, Geochimica et Cosmochimica Acta 60 (1996) 1727-1737.

[48] C. Le Losq, D. R. Neuville, P. Florian, G. S. Henderson and D. Massiot, The role of Al^{3+} on rheology and structural changes in sodium silicate and aluminosilicate glasses and melts, Geochimica et Cosmochimica Acta 126 (2014) 495–517.

[49] B. O. Mysen, L. W. Finger, D. Virgo and F. A. Seifert, Curve-fitting of Raman spectra of silicate glasses, American Mineralogist 67 (1982) 686-695.

[50] D. A. Long, Raman Spectroscopy (1977) McGraw-Hill, New York.

[51] A. Paul, J. D. Donaldson and M. J. K. Thomas, The ^{121}Sb Mössbauer spectra of antimony-containing glasses, Journal of Materials Science 12 (1977) 219-222.

[52] P. Charton and P. Armand, Glasses in the TeO_2–Sb_2O_4 binary system, Journal of Non-Crystalline Solids 316 (2003) 189–197.

[53] D. J. Stewart, O. Knop, C. Ayasse and F. W. D. Woodhams, Pyrochlores. VII. the oxides of antimony: an X-ray and Mössbauer study, Canadian Journal of Chemistry 50 (1972) 690-700.

[54] B. P. de Laune, G. J. Rees, M. J. Whitaker, H.-Y. Hah, C. E. Johnson, J. A. Johnson, D. E. Brown, M. G. Tucker, T. C. Hansen, F. J. Berry, J. V. Hanna and C. Greaves, Oxygen insertion reactions within the one-dimensional channels of phases related to $FeSb_2O_4$, Inorganic Chemistry 56 (2017) 594−607.

[55] P. A. Bingham, A. J. Connelly, N. C. Hyatt and R J. Hand, Corrosion of glass contact refractories for the vitrification of radioactive wastes: a review, International Materials Reviews 56 (2011) 226-242.

[56] C. Rubenstein, Factors for the calculation of the surface tension of glasses at 1200^{o}C, Glass Technology 5 (1964) 36-40.

[57] M. Imaoka, H. Hasegawa and S. Shindo, Properties and structure of glasses of B_2O_3-Sb_2O_3 system, Yogyo-Kyokai-Shi 77 (1969) 263-271.

[58] A. Fluegel, A. K. Varshneya, T. P. Seward and D. A. Earl, Viscosity of commercial glasses in the softening range, Ceramic Transactions 141 (2003) 379-386.

[59] T. Lakatos, Viscosity-temperature relations in glasses composed of SiO_2-Al_2O_3-Na_2O-K_2O-Li_2O-CaO-MgO-BaO-ZnO-PbO-B_2O_3, Glasteknisk Tidskrift 31 (1976) 51-54.

[60] A. Fluegel, Glass viscosity calculation based on a global statistical modelling approach, Glass Technol.: Eur. J. Glass Sci. Technol. A 48 (2007) 13-30.

[61] A. Fluegel, Global model for calculating room-temperature glass density from the composition, Journal of the American Ceramic Society 90 (2008) 2622-2625.

[62] S. A. Brawer and W. B. White, Raman spectroscopic investigation of the structure of silicate glasses. I. The binary alkali silicates, Journal of Chemical Physics 63 (1975) 2421-2432.

[63] S. A. Brawer and W. B. White, Raman spectroscopic investigation of the structure of silicate glasses. II. Soda-alkaline earth-alumina ternary and quaternary glasses, Journal of Non-Crystalline Solids 23 (1977) 261-278.

[64] D. R. Neuville, Viscosity, structure and mixing in (Ca, Na) silicate melts, Chemical Geology 229 (2006) 28-41.

[65] R. Limbach, S. Karlsson, G. Scannell, R. Mathew, M. Edén and L. Wondraczek, The effect of TiO_2 on the structure of Na_2O-CaO-SiO_2 glasses and its implications for thermal and mechanical properties, Journal of Non-Crystalline Solids 471 (2017) 6–18.

[66] E. Kilinc and R. J. Hand, Mechanical properties of soda–lime–silica glasses with varying alkaline earth contents, Journal of Non-Crystalline Solids 429 (2015) 190–197.

[67] N. Trcera, S. Rossano and M. Tarrida, Structural study of Mg-bearing sodosilicate glasses by Raman spectroscopy, Journal of Raman Spectroscopy 42 (2011) 765-772.

[68] O. N. Koroleva, V. N. Anfilogov, A. Shatskiy and K. D. Litasov, Structure of Na_2O–SiO_2 melt as a function of composition: in situ Raman spectroscopic study, Journal of Non-Crystalline Solids 375 (2013) 62–68.

[69] P. McMillan, Structural studies of silicate glasses and melts-applications and limitations of Raman spectroscopy, American Mineralogist 69 (1984) 622-644.

[70] H. Bradford, A. Ryder, J. Henderson and J. J. Titman, Structure of ancient glass by ^{29}Si magic angle spinning NMR spectroscopy, Chemistry a European Journal 24 (2018) 7474 – 7479.

[71] A. R. Jones, R. Winter, G. N. Greaves and I. H. Smith, MAS-NMR study of soda-lime-silicate glasses with variable degree of polymerisation, Journal of Non-Crystalline Solids 293-295 (2001) 87-92.

[72] K. Terashima, T. Hashimoto, T. Uchino, S.-H. Kim and T. Yoko, Structure and nonlinear optical properties of Sb_2O_3-B_2O_3 binary glasses, Journal of the Ceramic Society of Japan 104 (1996) 1008-1014.

[73] A. E. Miller, K. Nassau, K. B. Lyons and M. E. Lines, The intensity of Raman scattering in glasses containing heavy metal oxides, Journal of Non-Crystalline Solids 99 (1988) 289-307.

[74] D. Dorosz, J. Zmojda, M. Kochanowicz, P. Miluski, P. Jelen and M. Sitarz, Structural and optical study on antimony-silicate glasses doped with thulium ions, Spectrochimica Acta Part A: Molecular and Biomolecular Spectroscopy 134 (2015) 608–613.

[75] W. L. Konijnendijk and J. H. J. M. Buster, Raman-scattering measurements of silicate glasses containing sulphate, Journal of Non-Crystalline Solids 23 (1977) 401-418.

[76] T. Tsujimura, X. Xue, M. Kanzaki, M.J. Walter, Sulfur speciation and network structural changes in sodium silicate glasses: constraints from NMR and Raman spectroscopy, Geochimica et Cosmochimica Acta 68 (2004) 5081e5101.

[77] P. A. Bingham, S. Vaishnav, S. D. Forder, A. Scrimshire, B. Jaganathan, J. Rohini, J. C. Marra, K. M. Fox, E. M. Pierce, P. Workman and J. D. Vienna, Modelling the sulfate capacity of simulated radioactive waste borosilicate glasses, Journal of Alloys and Compounds 695 (2017) 656-667.

[78] M. Lenoir, A. Grandjean, S. Poissonnet and D. R. Neuville, Quantitation of sulfate solubility in borosilicate glasses using Raman spectroscopy, Journal of Non-Crystalline Solids 355 (2009) 1468–1473.

[79] S. Vaishnav, A. C. Hannon, E. R. Barney and P. A. Bingham, Neutron diffraction and Raman studies of the incorporation of sulfate in silicate glasses, Journal of Physical Chemistry C 124 (2020) 5409-5424.

[80] A. G. Kalampounias, S. N. Yannopoulos and G. N. Papatheodorou, Temperature induced structural changes in glassy, supercooled, and molten silica from 77 to 2150 K, Journal of Chemical Physics 124 (2006) 014504.

[81] A. G. Kalampounias, S. N. Yannopoulos and G. N. Papathedorou, A high-temperature Raman spectroscopic investigation of the potassium tetrasilicate in glassy, supercooled, and liquid states, Journal of Chemical Physics 125 (2006) 164502.

[82] P. McMillan and B. Piriou, Raman spectroscopy of calcium aluminate glasses and crystals, Journal of Non-Crystalline Solids 55 (1983) 221-242.

[83] L. Koudelka, J. Šubčík a, P. Mošner, L. Montagne and L. Delevoye, Structure and properties of Sb_2O_3-containing zinc borophosphate glasses, Journal of Non-Crystalline Solids 353 (2007) 1828–1833.

[84] R. E. Youngman, S. Sen, L. K. Cornelius and A. J. G. Ellison, Novel structural aspects of Sb_2O_3-B_2O_3 glasses, Physics and Chemistry of Glasses 44 (2003) 69-74.

[85] A. J. G. Ellison and S. Sen, Role of Sb^{3+} as a network-forming cation in oxide glasses, Physical Review B 67 (2003) 052203.

[86] L. A. Miller, H. St.C. O'Neill, A. J. Berry and C. J. Glover, The oxidation state and coordination environment of antimony in silicate glasses, Chemical Geology 524 (2019) 283-294.

[87] A. Schütz, D. Ehrt, M. Dubiel, X. Yang, B. Mosel and H. Eckert, A multi-method characterization of borosilicate glasses doped with 1 up to 10 mol% of Fe, Ti and Sb, Glastechnische Berichte: Glass Science and Technology 77 (2004) 295-305.

[88] W. D. Johnston, Oxidation-reduction equilibria in molten $Na_2O.2SiO_2$ glass, Journal of the American Ceramic Society 48 (1965) 184-190.

[89] A. W. M. de Best, Redox behaviour and fining of molten glass, PhD thesis, Technische Universiteit Eindhoven, Netherlands (1994). https://doi.org/10.6100/IR426291

[90] L. Backnaes and J. Deubener, Experimental studies on sulfur solubility in silicate melts at near-atmospheric pressure, Reviews in Mineralogy and Geochemistry 73 (2011) 143-165.

[91] L. Grund, B. Jonson and K. Lundstedt, The influence of basicity on oxygen activity and antimony oxide fining efficiency in alkali alkaline earth aluminosilicate glasses, Glass Technology: European Journal of Glass Science and Technology A 50 (2009) 241–246.

[92] P. Fredrickx, I. De Ryck, K. Janssens, D. Schryvers, J.-P. Petit and H. Döcking, EPMA and m-SRXRF analysis and TEM-based microstructure characterization of a set of Roman glass fragments, X-Ray Spectrometry 33 (2004) 326–333.

[93] I. C. Freestone and C. P. Stapleton, Composition, technology and production of coloured glasses from Roman mosaic vessels, Chapter 6 in: Glass of the Roman world, Ed. J. Bayley, I. Freestone and C. Jackson, Oxbow Books, Oxford (2015) 61-77.

[94] K. D. Kim, H. K. Kim and J. H. Kim, Behavior of oxygen equilibrium pressure in CRT glass melts doped with Sb and Ce ions from the viewpoint of fining, Journal of the Korean Ceramic Society 44 (2007) 419-423.

[95] H. Yamashita, S. Yamaguchi, R. Nishimura and T. Maekawa, Voltammetric studies of antimony ions in soda-lime-silica glass melts up to 1873K, Analytical Sciences 17 (2001) 45-50.

[96] S. Rada, L. Rus, M. Rada, M. Zagrai, E. Culea and T. Rusu, Compositional dependence of structure, optical and electrochemical properties of antimony (III) oxide doped lead glasses and vitroceramics, Ceramics International 40 (2014) 15711-15716.

[97] J. P. Allen, J. J. Carey, A. Walsh, D. O. Scanlon and G. W. Watson, Electronic structures of antimony oxides, Journal of Physical Chemistry C 117 (2013) 14759−14769.

[98] D. Xu, R. Wei, J. Cao and H. Guo, Luminescence and energy transfer of Sb^{3+}/Dy^{3+} co-doped magnesium sodium-phosphate glasses, Optical Materials Express 7 (2017) 2899-2904.

[99] W. Johansson, A. Peralta, B. Jonson, S. Anand, L. Österlund and S. Karlsson, Transparent TiO_2 and ZnO thin films on glass for UV protection of PV modules, Frontiers in Materials 6 (2019) 259.